Draft version January 27, 2011
Preprint typeset using LaTeX style emulateapj v. 11/10/09

arXiv:1101.4941v1 [astro-ph.CO] 25 Jan 2011

MID-INFRARED PROPERTIES OF OH MEGAMASER HOST GALAXIES. I. *SPITZER* IRS LOW- AND HIGH-RESOLUTION SPECTROSCOPY

Kyle W. Willett[1], Jeremy Darling[1], Henrik W. W. Spoon[2], Vassilis Charmandaris[3,4], & Lee Armus[5]

Draft version January 27, 2011

ABSTRACT

We present mid-infrared spectra and photometry from the Infrared Spectrograph on the *Spitzer Space Telescope* for 51 OH megamasers (OHMs), along with 15 galaxies confirmed to have no megamaser emission above $L_{OH} = 10^{2.3} L_{\odot}$. The majority of galaxies display moderate-to-deep 9.7 μm amorphous silicate absorption, with OHM galaxies showing stronger average absorption and steeper 20–30 μm continuum emission than non-masing galaxies. Emission from multiple polycyclic aromatic hydrocarbons (PAHs), especially at 6.2, 7.7, and 11.3 μm, is detected in almost all systems. Fine-structure atomic emission (including [Ne II], [Ne III], [S III], and [S IV]) and multiple H_2 rotational transitions are observed in more than 90% of the sample. A subset of galaxies show emission from rarer atomic lines, such as [Ne V], [O IV], and [Fe II]. 50% of the OHMs show absorption from water ice and hydrogenated amorphous carbon grains (HACs), while absorption features from CO_2, HCN, C_2H_2, and crystalline silicates are also seen in several OHMs. Column densities of OH derived from 34.6 μm OH absorption are similar to those derived from 1667 MHz OH absorption in non-masing galaxies, indicating that the abundance of masing molecules is similar for both samples. This data paper presents full mid-infrared spectra for each galaxy, along with measurements of line fluxes and equivalent widths, absorption feature depths, and spectral indices.

Subject headings: masers - galaxies: interactions - galaxies: nuclei - infrared: galaxies

1. INTRODUCTION

OH megamasers (OHMs) are 18-cm masers with integrated line luminosities on the order of $10^1 - 10^4$ $L_{\odot}$. They are an extremely rare phenomenon in the local universe, with roughly one hundred currently known out to a redshift of $z = 0.265$ (Baan et al. 1992). All OHMs, including the more powerful "gigamasers" ($L_{OH} > 10^4$ $L_{\odot}$) are associated with starburst nuclei in merging galaxies. OHMs have been identified in many different types of nuclear environments as classified by optical spectra, but the merging galaxies are without exception (ultra)luminous infrared galaxies ([U]LIRGs). Since OHMs are signposts of gas-rich merging galaxies, their presence can also indicate the existence of associated phenomena including massive black hole mergers and highly obscured circumnuclear starbursts (Darling 2007). OHMs are a powerful tool in this respect due in large part to their ability to be seen at cosmic distances. In order to employ OHMs as tracers, however, the assumption must be made that the OH line properties remain constant as a function of cosmic time and host environment. An explanation of the physical mechanisms and conditions responsible for distinguishing OHMs from non-masing ULIRGs is thus vital for understanding both the megamaser phenomenon and the associated merger characteristics.

Spectroscopic studies of the mid-IR emission in the host galaxies offer multiple diagnostics which can provide clues to the nature of the maser pumping mechanism and the associated OH emission. We used the Infrared Spectrograph (IRS) aboard the *Spitzer Space Telescope* (Werner et al. 2004) to study merging ULIRGs. Since the dusty nuclear regions are typically obscured at optical wavelengths, mid-IR observations can yield valuable information specific to the locations in which the OHMs are generated. These include measurements of the dust temperature and optical depth (from broadband photometry and absorption features), the excitation and temperature of the gas (molecular and fine-structure atomic lines), and high-ionization lines that can signal the presence of an active galactic nucleus (AGN), a possible heating source for the dust.

This data paper presents full low- and high-resolution IRS spectra along with measured mid-IR properties for 51 OHMs and 15 non-masing ULIRGs. An accompanying paper (Willett et al. 2011; Paper II) presents the full analysis, statistical comparisons of the masing and non-masing galaxies, and tests the viability of current OHM pumping models based on the IRS data.

2. THE SAMPLE

The OHM host galaxies selected for IRS observations were primarily drawn from the Arecibo OHM survey (Darling & Giovanelli 2002a,b). We selected well-studied OHMs with unambiguous maser detections and large amounts of ancillary data (including OH line and radio continuum maps, near-IR imaging, and optical imaging and spectroscopy) to maximize scientific return on the sample. A lower threshold of $L_{OH} > 10^{1.6}$ $L_{\odot}$ also eliminated extragalactic "kilomasers" from the sample, which

[1] Center for Astrophysics and Space Astronomy, Department of Astrophysical and Planetary Sciences, UCB 391, University of Colorado, Boulder, CO 80309-0391; willettk@colorado.edu
[2] Astronomy Department, Cornell University, Ithaca, NY 14853
[3] University of Crete, Department of Physics and Institute of Theoretical & Computational Physics, GR-71003, Heraklion, Greece
[4] IESL/Foundation for Research and Technology-Hellas, GR-71110, Heraklion, Greece; and Chercheur Associé, Observatoire de Paris, F-75014, Paris, France
[5] Spitzer Science Center, California Institute of Technology, Pasadena, CA 91125

are likely powered by different radiative processes than megamasers (Henkel & Wilson 1990).

In order to be detected in reasonable integration times using the IRS, we required that all potential targets have $S(60\ \mu\mathrm{m}) > 0.8$ Jy as measured by the IRAS satellite. After removing objects already observed by the IRS (largely through the GTO ULIRG program; *eg* Armus et al. 2007), we observed 24 galaxies in the redshift range $0.1 < z < 0.2$.

We supplemented these galaxies with additional spectra of OHM hosts publicly available through the *Spitzer* archive. To ensure uniformity of the data, we selected only galaxies from the archive that had full coverage with both the IRS low- and high-resolution modules. As of March 2008, the publicly available data from the archive yielded an additional 27 OHM galaxies (Table 1).

In order to provide a baseline for analysis of the OHMs, we also identified a control sample of ULIRGs that showed no megamaser emission above a firm limit. To identify these galaxies, we drew on non-detections from OH surveys by Baan et al. (1992); Staveley-Smith et al. (1992); Darling & Giovanelli (2000, 2001, 2002a) and Kent et al. (2002). The upper limit for OH emission is conservatively derived from the rms noise in the spectrum at 1667 MHz, assuming a boxcar line profile with a linewidth $\Delta v = 150$ km/s and a 1.5σ detection:

$$L_{OH}^{max} = 4\pi D_L^2 (1.5\sigma) \left(\frac{\Delta v}{c}\right) \left(\frac{\nu_0}{1+z}\right) \qquad (1)$$

For this control sample, we set an upper limit of $L_{OH}^{max} < 10^{2.3}\ L_\odot$; this limit compromises between ensuring that all but the faintest megamaser emission is excluded and yielding a reasonable number of objects in the control sample for statistical analysis. All 51 OHMs in our IRS sample have L_{OH} above this limit.

In addition to selecting galaxies based on OH non-detection, we imposed two additional criteria to ensure that the control sample was as similar as possible to the OHM hosts. Firstly, we set a lower limit on the far-infrared luminosity (Sanders & Mirabel 1996) of the non-masing galaxies as measured by their IRAS fluxes. OHMs occur exclusively in IR-bright galaxies, due to the fact that the maser is pumped primarily by rotational transitions of a few hundred K above the ground state (Baan et al. 1982; Henkel et al. 1987). Darling & Giovanelli (2002a) show that the relationship between the OH and infrared luminosities is a power law with $L_{OH} \propto L_{FIR}^{1.2}$. Since no OHM observed with the IRS has $L_{FIR} < 10^{11} L_\odot$, we established this as the lower limit for inclusion in the non-masing sample.

Secondly, a cutoff in redshift space is applied to sample a sufficiently large volume ($V \sim 1$ Gpc^3) in order to avoid systematic effects such as the Malmquist bias. The available data in the archive contained many more galaxies at lower redshifts ($z < 0.05$) than those further away. To avoid over-weighting the control sample towards galaxies at low redshifts, we sorted galaxies that met the L_{OH}^{max} and L_{IR} criteria into bins of $\Delta\ z = 0.02$. For bins where the number of non-masing galaxies exceeded those of OHMs, we randomly removed objects from the non-masing bins until the numbers were equal. This reduced the control sample to 1 galaxy at $0 < z < 0.02$ and 4 galaxies at $0.02 < z < 0.04$; for all other redshift bins, no such adjustments were necessary. As of March 2008, there existed 15 suitable candidates in the *Spitzer* archive qualifying for the non-masing control sample (Table 1). Figure 1 shows the distribution of OH luminosity for all objects as a function of redshift; for the non-masing galaxies, we display upper limits as computed in Equation 1.

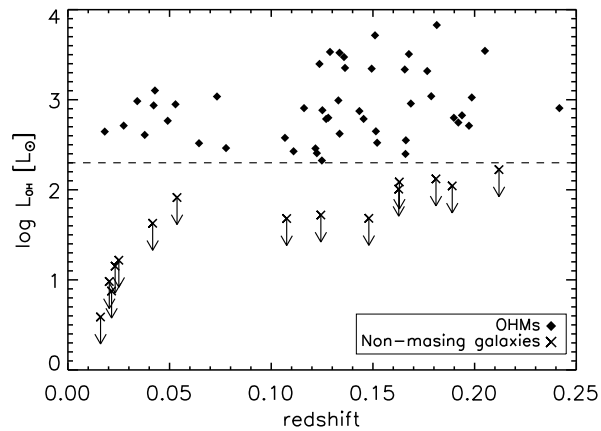

FIG. 1.— Distribution of integrated OH luminosity for the IRS samples as a function of redshift. For non-masing galaxies, the OH luminosity is an upper limit calculated from Equation 1. The dashed line at $L_{OH} = 10^{2.3}\ L_\odot$ is the upper limit on possible OH emission for the non-masing control sample.

Throughout this paper, we assume the WMAP5 cosmology with $H_0 = 70.5$, $\Omega_M = 0.274$, and $\Omega_\Lambda = 0.726$ (Hinshaw et al. 2009).

3. OBSERVATIONS

We observed 24 OHMs with the IRS from August 2006 through December 2007. The IRS contains four modules in two different spectroscopic resolutions: low- (LR) and high-resolution (HR) (Houck et al. 2004). The short-high (SH) and long-high (LH) modules operate at a resolution of $R \sim 600$; the short-low (SL1 & SL2) and long-low (LL1 & LL2) modules operate at resolutions ranging from $R \sim 56 - 127$, depending on the observing wavelength. Two orders, SL3 ($7.3 - 8.7\ \mu$m) and LL3 ($19.4 - 21.7\ \mu$m), cover the overlapping range between the first and second orders in both SL and LL. We used these only as checks for the absolute flux calibration between the different orders.

All targets used the Staring Mode Astronomical Observing Template (AOT) with the galaxies placed at two nod positions approximately one-third and two-thirds the length of the slit. We observed targets in all six modules as well as an equal-time, off-target exposure in the LH module to be used for sky subtraction.

Although the majority of our sources had no previous IRAS detections in either the 12 or 25 μm bands, we extrapolated the likely flux based on the colors of ULIRGs at similar redshifts and the measured fluxes at 60 μm. We chose cycle times intended to yield signal-to-noise ratios of $S/N = 50 - 100$ for the low-resolution modules and $S/N \geq 10$ for the high-resolution modules, allowing for accurate measurement of faint emission and absorption features, as well as accurate spectral decomposition.

For the 24 objects in the dedicated OHM program, we took dedicated sample-up-the-ramp (SUR) peakup ob-

TABLE 1
Radio, optical, and FIR properties of OHMs and non-masing galaxies

	IRAS FSC	RA J2000.0	Dec J2000.0	$z_{\odot}$ [a]	D_L [h_{70}^{-1} Mpc]	log L_{FIR} [b] [$h_{70}^{-2} L_{\odot}$]	log L_{OH} [c] [$h_{70}^{-2} L_{\odot}$]	$f_{1.4\ GHz}$ [d] [mJy]	Alt. desig.
OHMs	IRAS 01355−1814	01 37 57.4	−17 59 21	0.191	929	12.49	2.75	< 5.0	
	IRAS 01418+1651	01 44 30.5	+17 06 05	0.0274	115	11.63	2.71	40.6	III Zw 035
	IRAS 01562+2528	01 59 02.6	+25 42 37	0.1658	788	12.19	3.31	6.3	
	IRAS 02524+2046	02 55 17.1	+20 58 43	0.1815	873	12.07−12.54	3.80	2.9	
	IRAS 03521+0028	03 54 42.2	+00 37 03	0.1522	718	12.59	2.49	6.7	
	IRAS 04121+0223	04 14 47.1	+02 30 36	0.1216	568	11.69−11.96	2.39	3.1	
	IRAS 04454−4838	04 46 49.5	−48 33 33	0.0529	235	11.89	2.95	< 5.0	ESO 203-IG 001
	IRAS 06487+2208	06 51 45.8	+22 04 27	0.1437	678	12.34	2.87	10.8	
	IRAS 07163+0817	07 19 05.5	+08 12 07	0.1107	515	11.79	2.43	3.5	
	IRAS 07572+0533	07 59 57.2	+05 25 00	0.1894	926	12.31	2.80	5.0	
	IRAS 08201+2801	08 23 12.6	+27 51 40	0.1680	808	12.26	3.51	16.7	
	IRAS 08449+2332	08 47 51.0	+23 21 06	0.1510	723	12.05	2.65	6.1	
	IRAS 08474+1813	08 50 18.3	+18 02 01	0.1450	692	12.19	2.76	4.2	
	IRAS 09039+0503	09 06 34.2	+04 51 25	0.1250	589	12.16	2.88	6.6	
	IRAS 09539+0857	09 56 34.3	+08 43 06	0.1290	608	12.09	3.53	9.5	
	IRAS 10035+2740	10 06 26.3	+27 25 46	0.1662	794	12.26	2.55	6.3	
	IRAS 10039−3338	10 06 04.8	−33 53 15	0.0341	154	11.74	2.98	24.7	
	IRAS 10173+0828	10 20 00.2	+08 13 34	0.0480	222	11.86	2.77	10.8	
	IRAS 10339+1548	10 36 37.9	+15 32 42	0.1965	969	12.35	2.71	5.1	
	IRAS 10378+1109	10 40 29.2	+10 53 18	0.1362	646	12.35	3.35	8.9	
	IRAS 10485−1447	10 51 03.1	−15 03 22	0.1330	629	12.23	2.99	4.4	
	IRAS 11028+3130	11 05 37.5	+31 14 32	0.1990	975	12.39	3.03	5.0	
	IRAS 11180+1623	11 20 41.7	+16 06 57	0.1660	801	12.27	2.40	4.2	
	IRAS 11524+1058	11 55 02.8	+10 41 44	0.1784	868	12.19	3.04	5.0	
	IRAS 12018+1941	12 04 24.5	+19 25 10	0.1687	814	12.48	2.96	6.5	
	IRAS 12032+1707	12 05 47.7	+16 51 08	0.2170	1082	12.64	4.21	28.7	
	IRAS 12112+0305	12 13 46.0	+02 48 38	0.0730	335	12.38	3.04	23.8	
	IRAS 12540+5708	12 56 14.2	+56 52 25	0.0422	188	12.42	2.94	309.9	Mrk 231
	IRAS 13218+0552	13 24 19.9	+05 37 05	0.2051	1011	12.44	3.50	5.3	
	IRAS 13428+5608	13 44 42.1	+55 53 13	0.0378	167	12.18	2.61	145.4	Mrk 273
	IRAS 13451+1232	13 47 33.3	+12 17 24	0.1220	571	12.21	2.46	5398.0	4C +12.50
	IRAS 14059+2000	14 08 18.7	+19 46 23	0.1237	580	11.94	3.40	7.5	
	IRAS 14070+0525	14 09 31.2	+05 11 32	0.2644	1346	12.87	4.50	5.2	
	IRAS 14553+1245	14 57 43.4	+12 33 16	0.1249	585	11.87	2.33	3.8	
	IRAS 15327+2340	15 34 57.1	+23 30 11	0.0181	80	12.22	2.65	326.8	Arp 220
	IRAS 16090−0139	16 11 40.5	−01 47 06	0.1339	628	12.57	3.52	20.9	
	IRAS 16255+2801	16 27 38.1	+27 54 52	0.1340	627	11.94	2.62	5.0	
	IRAS 16300+1558	16 32 21.4	+15 51 45	0.2417	1212	12.80	2.91	7.9	
	IRAS 17207−0014	17 23 21.9	−00 17 01	0.0428	188	12.45	3.10	82.4	
	IRAS 18368+3549	18 38 35.4	+35 52 20	0.1162	536	12.24	2.91	21.0	
	IRAS 18588+3517	19 00 41.2	+35 21 27	0.1067	489	11.92	2.58	5.9	
	IRAS 20100−4156	20 13 29.5	−41 47 35	0.1296	603	12.68	4.13	< 5.0	
	IRAS 20286+1846	20 30 55.5	+18 56 46	0.1347	633	12.06	3.47	5.0	
	IRAS 21077+3358	21 09 49.0	+34 10 20	0.1764	846	12.10−12.24	3.32	9.4	
	IRAS 21272+2514	21 29 29.4	+25 27 50	0.1508	709	11.99−12.14	3.71	4.4	
	IRAS 22055+3024	22 07 49.7	+30 39 40	0.1269	587	12.19	2.79	6.4	
	IRAS 22116+0437	22 14 09.9	+04 52 24	0.1939	937	12.12−12.32	2.83	8.4	
	IRAS 22491−1808	22 51 49.2	−17 52 23	0.0778	346	12.19	2.46	5.9	
	IRAS 23028+0725	23 05 20.4	+07 41 44	0.1496	701	11.86−12.06	3.34	19.5	
	IRAS 23233+0946	23 25 56.2	+10 02 49	0.1279	591	12.18	2.80	11.6	
	IRAS 23365+3604	23 39 01.3	+36 21 09	0.0645	283	12.19	2.52	28.7	
Non-masing	IRAS 00164−1039	00 18 50.4	−10 22 08	0.0272	113	11.36	< 1.25	< 5.0	Arp 256
	IRAS 01572+0009	01 59 50.2	+00 23 41	0.1630	774	12.47	< 2.12	26.7	Mrk 1014
	IRAS 05083+7936	05 16 46.4	+79 40 13	0.0537	237	11.93	< 1.94	41.4	
	IRAS 06538+4628	06 57 34.4	+46 24 11	0.0214	93.6	11.24	< 0.89	64.3	UGC 3608
	IRAS 08559+1053	08 58 41.8	+10 41 22	0.1480	705	12.18	< 1.72	< 5.0	
	IRAS 09437+0317	09 46 20.6	+03 03 30	0.0205	93.5	11.15	< 1.01	< 5.0	
	IRAS 10565+2448	10 59 18.1	+24 32 34	0.0431	194	12.04	< 1.66	57.0	
	IRAS 11119+3257	11 14 38.9	+32 41 33	0.1890	923	12.48	< 2.07	110.4	
	IRAS 13349+2438	13 37 18.7	+24 23 03	0.1076	500	11.39	< 1.72	20.0	
	IRAS 15001+1433	15 02 31.9	+14 21 35	0.1627	781	12.42	< 2.04	16.9	
	IRAS 15206+3342	15 22 38.0	+33 31 36	0.1244	582	12.13	< 1.75	11.2	
	IRAS 20460+1925	20 48 17.3	+19 36 54	0.1807	868	12.03	< 2.15	18.9	
	IRAS 23007+0836	23 03 15.6	+08 52 26	0.0163	64.9	11.43	< 0.63	181.0	NGC 7469
	IRAS 23394−0353	23 42 00.8	−03 36 55	0.0232	95.4	11.11	< 1.18	< 5.0	Arp 295B
	IRAS 23498+2423	23 52 26.0	+24 40 17	0.2120	1037	12.44	< 2.25	6.8	

[a] Heliocentric optical redshift (Darling & Giovanelli 2002a).
[b] Computed according to the prescription of Sanders & Mirabel (1996), with a scale factor of $C = 1.6$. IRAS photometry is from Sanders et al. (2003); a range in L_{FIR} means that the object was not detected by IRAS at 100 μm.
[c] OH fluxes are from Darling & Giovanelli (2002a,b); limits are computed according to Eqn. 1.
[d] Flux densities at 1.4 GHz are from the NRAO VLA Sky Survey (Condon et al. 1998).

servations in both the blue (16 μm) and red (22 μm) filters in sample-up-the-ramp (SUR) mode for photometric calibration of the spectra. The SUR peakups did not coincide in time with the spectroscopy for the majority of targets. None of the galaxies selected from the *Spitzer* archive possessed SUR peakup data; 16 archived galaxies have double correlated sampling (DCS) peakups with slightly worse photometric accuracy than those with SUR data. Only one galaxy, IRAS 10173+0828, had no peakup observations of any kind. Measured peakup fluxes are given in Table 3.

The *Spitzer* beam is diffraction limited past 6 μm, with slit widths for the spectral modules between $3-11''$. The vast majority of the nuclei in merging ULIRGs have angular separations less than the instrument PSF, and thus can be treated as point sources. For the few galaxies close enough to be resolved, we chose staring mode observations centered on the IR-dominant nuclear region of the galaxy. The only available observations of the double nucleus in IRAS 10485−1447 were centered on the western nucleus. Details of the IRS observations are given in Table 2.

4. DATA REDUCTION

4.1. *Dedicated observations of OHM galaxies*

The data were processed using the *Spitzer* Science Center S17.0 data pipeline. We used basic calibrated data (BCD) products for our analysis, having already been corrected for flat-fielding, stray light contributions, nonlinear responsivity in the pixels, and "drooping" (an increase in detector pixel voltage that occurs during nondestructive readouts). The 2-D BCD images were first medianed over the data cycles at each nod position to remove transient effects such as cosmic rays. For the SL and LL modules, we subtracted the sky contribution by differencing the BCD images for each nod position with the adjacent position in the same module.

The slit sizes of the SH and LH modules are too small to permit extraction of a sky background during the same observation. The continuum levels in the high-resolution modules, however, contain strong contributions from scattered zodiacal light. Estimations of the flux at 15 μm using SPOT predict zodi contributions within the *Spitzer* beam ranging from 20–80 mJy, which in many cases is of comparable magnitude to the expected signal from the galaxies themselves. The wavelength-dependent brightness of the sky contribution means that it cannot be corrected using a simple scaling, and so we did not attempt to further calibrate either HR module. The calibrated low-resolution spectra were thus used for absolute fluxes and the high-resolution spectra for line ratio diagnostics (which are unaffected by continuum levels).

To obtain more accurate measurements of faint lines at longer wavelengths, we took dedicated off-source sky observations in the LH module for all 24 OHMs in our program. Subtraction of the wavelength-dependent background, however, significantly affected the measured line fluxes. For galaxies with background subtraction in only the LH module, this changes the line ratios measured between different HR modules (*eg*, [S III]λ33/[S IV]λ10.5). We reduced the data both with and without subtraction of the sky backgrounds; the background-subtracted LH spectra are attached as an appendix.

Following the initial cleaning of the 2-D BCD products, we eliminated rogue pixels using the IDL package IRSCLEAN_MASK[1]. We used rogue pixel masks provided by the SSC for each IRS campaign, and supplemented the standard masks with manual cleaning of each nod and module. The 1-D spectra were then extracted using the Spitzer IRS Custom Extractor (SPICE) v.2.0. For all modules we used the optimal extraction routine with the standard aperture to improve the S/N ratio in faint galaxies.

The low-resolution modules were stitched together to match continuum levels by using a multiplicative scaling. We fixed the LL1 module and then scaled LL2 to LL1, SL1 to LL2, and SL2 to SL1. The mean scaling factors were 1.03 ± 0.08 for LL2 to LL1, 1.49 ± 0.69 for SL1 to LL2, and 1.37 ± 0.78 for SL2 to SL1. We then calibrated the entire low-resolution spectra as a single unit by scaling to the IRS 22 μm sample-up-the-ramp (SUR) peakups. The required scaling in the majority of cases was quite small, indicating that the sky subtraction and spectral extraction techniques are robust; the mean scaling factor was 0.94 ± 0.08. The accuracy of the overall continuum flux calibration is $\sim 5\%$ (Houck et al. 2004).

Noisy areas on both ends of the SH and LH orders were trimmed from the 1-D spectra. These areas typically encompass a range of 10–30 pixels on the edges of the orders and correspond to areas of decreased sensitivity on the detector. We deliberately trimmed only pixels with an overlapping wavelength range in adjacent orders so that a maximum amount of information is preserved. In isolated cases, we also removed obvious rogue pixels by hand from spectra in which exceptional 1-channel features appear in only a single nod.

We calculated a simple figure of merit to measure the signal-to-noise ratio in the low-resolution data. The data near $\lambda_{rest} = 21$ μm (a feature-free area near the center of most spectra) are fit with a low-order polynomial; the median flux in that region is then divided by the rms noise to yield the S/N (Table 3). We note that this parameter is a function of wavelength, as well as the performance and integration time in each spectral module; this is intended to give only a rough estimate for each object. The S/N for the samples ranges from $\sim 10-110$, with a median of 35.

4.2. *Archival data*

Since the archival OHM and non-masing galaxies did not come from a unified observing program, the version of the *Spitzer* data pipeline and the level of processing varied slightly from object to object - we used the most recent versions available in the archive (v15.3.0 or later). The reduction process was identical to that for the OHM galaxies in our program, with the exception of the LR photometric scaling; since observations in the archive varied in availability of peakup data, we used a variety of sources to calibrate the spectra. In order of priority, we used the IRS dedicated 22 μm SUR peakups, IRS acquisition 16 and 22 μm DCS peakups, or IRAS 25 μm observations (all lying within the coverage of the

[1] IRSCLEAN_MASK is available at `http://ssc.spitzer.caltech.edu/archanaly/contributed/irsclean/IRSCLEAN_MASK.html`

TABLE 2
IRS OBSERVATION LOG

Object	Date	Peakup type	SL1	SL2	LL1	LL2	SH	LH	Program
IRAS 01355−1814		BPU-offset	60 × 2	60 × 2	30 × 2	30 × 2	120 × 4	240 × 5	4,6
IRAS 01418+1651		BPU	14 × 2	14 × 2	14 × 4	14 × 4	120 × 5	60 × 7	2,3
IRAS 01562+2528	2007 Sep 09	BPU-offset	14 × 7	14 × 7	30 × 3	30 × 3	120 × 2	60 × 2	1
IRAS 02524+2046	2007 Sep 09	BPU	14 × 7	14 × 7	30 × 3	30 × 3	120 × 2	60 × 2	1
IRAS 03521+0028		BPU-offset	60 × 2	60 × 2	30 × 3	30 × 3	120 × 3	60 × 4	4
IRAS 04121+0223	2007 Oct 05	BPU-offset	60 × 2	60 × 2	30 × 3	30 × 3	120 × 2	60 × 2	1
IRAS 04454−4838		BPU	60 × 2	60 × 2	30 × 3	30 × 3	120 × 3	240 × 2	3
IRAS 06487+2208	2007 May 04	BPU-offset	14 × 7	14 × 7	30 × 3	30 × 3	120 × 2	60 × 2	1
IRAS 07163+0817	2007 May 03	BPU	14 × 6	14 × 6	30 × 3	30 × 3	120 × 2	60 × 2	1
IRAS 07572+0533	2007 May 04	BPU	14 × 6	14 × 6	30 × 3	30 × 3	120 × 2	60 × 2	1
IRAS 08201+2801	2007 May 03	BPU-offset	14 × 7	14 × 7	30 × 3	30 × 3	120 × 2	60 × 2	1
IRAS 08449+2332	2007 May 04	BPU-offset	14 × 6	14 × 6	30 × 3	30 × 3	120 × 2	60 × 2	1
IRAS 08474+1813	2007 Dec 05	BPU	14 × 6	14 × 6	30 × 3	30 × 3	120 × 2	60 × 2	1
IRAS 09039+0503		BPU	60 × 2	60 × 2	30 × 4	30 × 4	120 × 4	240 × 3	5,6
IRAS 09539+0857		BPU	60 × 2	60 × 7	30 × 4	30 × 4	120 × 3	240 × 3	5,6
IRAS 10035+2740	2007 Jun 09	BPU-offset	14 × 7	14 × 7	30 × 3	30 × 3	120 × 2	60 × 2	1
IRAS 10039−3338		BPU	14 × 6	14 × 6	14 × 4	14 × 4	30 × 6	60 × 2	3
IRAS 10173+0828		none	60 × 1	60 × 1	14 × 4	14 × 4	120 × 4	60 × 12	3,7,8
IRAS 10339+1548	2007 Jun 08	BPU-offset	14 × 7	14 × 7	30 × 3	30 × 3	120 × 2	60 × 2	1
IRAS 10378+1109		BPU-offset	60 × 2	60 × 2	30 × 3	30 × 3	120 × 3	60 × 4	4
IRAS 10485−1447		BPU	60 × 2	60 × 2	30 × 4	30 × 4	120 × 2	240 × 2	5,6
IRAS 11028+3130	2007 Jun 09	BPU-offset	60 × 2	60 × 2	30 × 3	30 × 3	120 × 2	60 × 2	1
IRAS 11180+1623	2007 Jun 08	BPU-offset	14 × 7	14 × 7	30 × 3	30 × 3	120 × 2	60 × 2	1
IRAS 11524+1058	2007 Jun 12	BPU-offset	14 × 7	14 × 7	30 × 3	30 × 3	120 × 2	60 × 2	1
IRAS 12018+1941		BPU-offset	60 × 1	60 × 1	30 × 3	30 × 3	120 × 3	60 × 4	4
IRAS 12032+1707		BPU-offset	60 × 2	60 × 2	30 × 2	30 × 2	120 × 3	240 × 3	4,6
IRAS 12112+0305		BPU-offset	14 × 3	14 × 3	30 × 2	30 × 2	120 × 2	60 × 4	4
IRAS 12540+5708		BPU	14 × 2	14 × 2	6 × 5	6 × 5	30 × 6	60 × 4	9
IRAS 13218+0552		BPU-offset	60 × 1	60 × 1	30 × 3	30 × 3	120 × 3	60 × 4	4
IRAS 13428+5608		BPU	14 × 2	14 × 2	14 × 2	14 × 2	30 × 6	60 × 4	4
IRAS 13451+1232		BPU	14 × 3	14 × 3	30 × 2	30 × 2	30 × 6	60 × 4	4
IRAS 14059+2000	2007 Jul 31	BPU-offset	60 × 2	60 × 2	30 × 3	30 × 3	120 × 2	60 × 2	1
IRAS 14070+0525		BPU-offset	60 × 2	60 × 2	30 × 2	30 × 2	120 × 3	240 × 2	4
IRAS 14553+1245	2007 Jul 31	BPU	60 × 2	60 × 2	30 × 3	30 × 3	120 × 2	60 × 2	1
IRAS 15327+2340		BPU	14 × 3	14 × 3	6 × 5	6 × 5	30 × 6	60 × 4	10
IRAS 16090−0139		BPU-offset	60 × 1	60 × 1	30 × 3	30 × 3	120 × 2	60 × 4	4
IRAS 16255+2801	2006 Sep 17	BPU	60 × 2	60 × 2	30 × 3	30 × 3	120 × 2	60 × 2	1
IRAS 16300+1558		BPU-offset	60 × 2	60 × 2	30 × 5	30 × 5	120 × 4	240 × 4	4,6
IRAS 17207−0014		BPU	14 × 3	14 × 3	14 × 3	30 × 2	30 × 6	60 × 4	4
IRAS 18368+3549	2007 May 01	BPU	60 × 2	60 × 2	30 × 3	30 × 3	120 × 2	60 × 2	1
IRAS 18588+3517	2006 Nov 20	BPU	60 × 2	60 × 2	30 × 3	30 × 3	120 × 2	60 × 2	1
IRAS 20100−4156		BPU-offset	60 × 1	60 × 1	30 × 2	30 × 2	120 × 2	60 × 4	4
IRAS 20286+1846	2006 Nov 20	BPU	60 × 2	60 × 2	30 × 3	30 × 3	120 × 2	60 × 2	1
IRAS 21077+3358	2007 Jun 13	BPU	60 × 2	60 × 2	30 × 3	30 × 3	120 × 2	60 × 2	1
IRAS 21272+2514		BPU-offset	60 × 2	60 × 2	30 × 3	30 × 3	120 × 2	240 × 1	4,11
IRAS 22055+3024	2007 Jun 27	BPU	60 × 2	60 × 2	30 × 3	30 × 3	120 × 2	60 × 2	1
IRAS 22116+0437	2006 Dec 21	BPU-offset	60 × 2	60 × 2	30 × 3	30 × 3	120 × 2	60 × 2	1
IRAS 22491−1808		BPU-offset	60 × 1	60 × 1	30 × 2	30 × 2	120 × 2	60 × 4	4
IRAS 23028+0725	2006 Dec 20	BPU	14 × 7	14 × 7	30 × 3	30 × 3	120 × 2	60 × 2	1
IRAS 23233+0946		BPU	60 × 2	60 × 2	30 × 4	30 × 4	120 × 5	240 × 4	5,6
IRAS 23365+3604		BPU	14 × 3	14 × 3	30 × 2	30 × 2	30 × 6	60 × 4	4
IRAS 00163−1039		BPU	14 × 3	14 × 3	14 × 2	14 × 2	30 × 3	60 × 2	3
IRAS 01572+0009		BPU	14 × 3	14 × 3	30 × 2	30 × 2	30 × 6	60 × 4	4
IRAS 05083+7936		BPU	14 × 6	14 × 6	14 × 4	14 × 4	30 × 6	60 × 2	3
IRAS 06538+4628		BPU	14 × 3	14 × 3	14 × 2	14 × 2	30 × 3	60 × 2	3
IRAS 08559+1053		BPU-offset	60 × 2	60 × 2	30 × 3	30 × 3	120 × 3	60 × 4	12
IRAS 09437+0317		BPU	60 × 2	60 × 2	30 × 3	30 × 3	120 × 3	240 × 2	3
IRAS 10565+2448		BPU	14 × 3	14 × 3	30 × 2	30 × 2	30 × 6	60 × 4	4
IRAS 11119+3257		BPU	60 × 1	60 × 1	30 × 3	30 × 3	120 × 3	60 × 4	4
IRAS 13349+2438		BPU	14 × 5	14 × 5	14 × 5	14 × 5	120 × 5	60 × 10	13
IRAS 15001+1433		BPU-offset	60 × 2	60 × 2	30 × 3	30 × 3	120 × 3	60 × 4	4
IRAS 15206+3342		BPU-offset	60 × 1	60 × 1	30 × 3	30 × 3	120 × 3	60 × 4	4
IRAS 20460+1925		BPU	14 × 5	14 × 5	14 × 5	14 × 5	120 × 5	60 × 10	13
IRAS 23007+0836		BPU	14 × 2	14 × 2	6 × 5	6 × 5	30 × 4	60 × 2	14
IRAS 23394−0353		BPU	30 × 6	30 × 6	60 × 2	60 × 2	14 × 6	14 × 4	3
IRAS 23498+2423		BPU-offset	60 × 2	60 × 2	30 × 2	30 × 2	120 × 3	240 × 2	4

NOTE. — *Spitzer* archival data are from programs: (1) 30407 (PI: J. Darling); (2) - 3237 (PI: E. Sturm); (3) - 30323 (PI: L. Armus); (4) - 105 (PI: J. Houck); (5) - 2306 (PI: M. Imanishi); (6) - 3187 (PI: S. Veilleux); (7) - 3605 (PI: C. Bradford); (8) - 20549 (PI: R. Joseph); (9) - 1442 (PI: L. Armus); (10) - 1444 (PI: L. Armus); (11) - 20375 (PI: L. Armus); (12) - 666 (PI: J. Houck); (13) - 61 (PI: G. Rieke); (14) - 14 (PI: J. Houck). Exposure times for all modules are given as seconds per cycle × number of cycles.

LL modules). For galaxies from the archive, 17 are calibrated with DCS peakups, 21 with IRAS 25 μm photometry, and 4 are left uncalibrated. The mean scaling factor for the objects without SUR photometry was 1.05 ± 0.25, slightly higher than the mean scaling for galaxies in the dedicated OHM program.

Five OHMs and five non-masing galaxies from the archive had both SH and LH sky backgrounds taken simultaneously with the spectroscopic observations; the remainder had no high-resolution sky backgrounds in either module. Since we emphasize uniformity of the observations to the fullest extent possible, all data used for statistical comparisons between the samples use data *without* HR sky subtraction; line measurements for the background-subtracted objects are given in the Appendix.

The spectra for IRAS 20460+1925 and IRAS 23028+0725 had no flux in the SL modules, most likely due to a pointing error during observations. No SL data from either galaxy are used in our analyses here or in Paper II.

5. RESULTS

We show examples of the peakup-scaled low-resolution spectra for the OHMs in Figure 2, with the individual modules stitched together and bonus orders removed. Examples of the high-resolution SH and LH data are shown in Figures 3 and 4; full spectra for all galaxies are available as an online supplement. While individual orders within the high-resolution modules are typically well-aligned in flux, the differences in calibration between the SH and LH modules are clearly apparent when matching the spectra; this is due to a combination of different slit sizes for the SH and LH modules (a factor of ~ 4) and the lack of separate sky subtraction for the SH modules. For this reason, as well as emphasizing the narrow atomic and molecular features visible in the high-resolution spectra, we display separate plots for the SH and LH modules.

A small amount of the archival objects have previously published full IRS spectra (Armus et al. 2004; Weedman et al. 2005; Armus et al. 2007), mainly consisting of bright, nearby galaxies. Farrah et al. (2007) published HR spectra for roughly half of our archival OHM hosts. While many papers use the available data from the GTO programs, however, the majority of objects extracted from the archive have *no* published spectra, although some data are used in larger studies of ULIRG properties (*eg*, Higdon et al. 2006; Desai et al. 2007; Hao et al. 2007). The spectra for many of the archival galaxies are thus presented here for the first time.

Comparison of our data with the few spectra of objects previously published (*eg*, Mrk 1014, Arp 220, NGC 7469) revealed no significant differences in spectral shape or detection of individual features. Measurements of line flux and equivalent widths, however, may be affected by the photometric scaling and/or line-fitting routines used; for this reason, we chose to reduce *all* data in a uniform matter.

For many of our high-resolution spectra, especially those with low S/N, there exist individual spikes that do not correspond to any identified feature (see IRAS 01562+2528 for a prominent example). These features are typically 1–2 channels wide, much narrower than the expected linewidth for an unresolved feature. We regard such features as spurious, possibly caused by hot pixels or other instrumental conditions that are not corrected by our cleaning routines. All features we regard as valid detections are listed in the data tables, with the locations of the most common features marked on the spectra themselves.

5.1. *Continuum*

The continuum emission for all objects in the OHM sample has a relatively homogenous spectral shape over the range of the IRS, although differences in spectral shape between the two samples do appear and are explored in Paper II. Figure 5 shows the individual objects overlaid with a template generated by medianing the flux in each wavelength bin from *all* galaxies. The template bears a close resemblance to starbursting ULIRG spectra seen in previous surveys (Hao et al. 2007; Weedman & Houck 2009). The LR spectrum clearly shows silicate absorption at 9.7 and 18 μm and water ice absorption at 6 μm. Low-resolution emission features are dominated by the broad PAH features from 6–13 μm, with weaker contibutions from neon, sulfur, and molecular hydrogen also visible.

The continuum data from $\lambda_{rest} = 20 - 30$ μm is in most cases well-characterized by a power-law fit, with the short wavelength break occurring near the 18 μm silicate feature and the long wavelength end cut off by the spectral range of the IRS. Shortward of 15 μm, the continuum becomes increasingly contaminated by individual absorption and emission features, especially from PAH emission and the deep silicate absorption at 9.7 μm. Following Brandl et al. (2006), we fit a spectral index to the continuum in two components, with α_{30-20} measuring the relatively feature-free flux from $20 - 30$ μm and α_{15-6} measuring the contribution from $5.3 - 14.8$ μm; the wavelengths are slightly shifted to avoid contamination from water ice at 6 μm and [Ne III] at 15.6 μm (Table 3).

The mean 15-6 spectral index for the entire OHM sample is $\alpha_{15-6} = 2.1 \pm 0.6$; the mean 30-20 slope is $\alpha_{30-20} = 4.8 \pm 1.1$. The shallowest 15-6 slope occurs for IRAS 10039−3338 ($\alpha_{15-6} = -0.1$), an object with weak PAH features and very strong silicate absorption; the steepest index occurs for IRAS 12018+1941 ($\alpha_{15-6} = 3.0$), which has moderate PAH and line emission features and a nearly constant spectral index over the entire mid-IR range. Steeper 15-6 indices are likely due to a combination of smaller relative quantities of warm dust (thermal blackbodies of ~ 300 K peaking near 10 μm) and larger quantities of cooler dust.

The shallowest 30-20 slope occurs for IRAS 13451+1232 ($\alpha_{30-20} = 1.9$); the low-resolution spectrum for this object more closely resembles that seen in Seyfert galaxies and PG quasars (Schweitzer et al. 2006; Hao et al. 2007), with weak PAH emission and shallower silicate absorption. The continuum emission for this object is also much closer to being uniform over the entire range of the IRS; the difference between the two spectral indices is only $\Delta\alpha = -0.4$, compared to an average of $\Delta\alpha = 2.7$ for the entire sample. This behavior is more typical of non-thermal emission that can extend over many decades with the same index. The steepest 30-20 emission measured is from IRAS 11028+3130

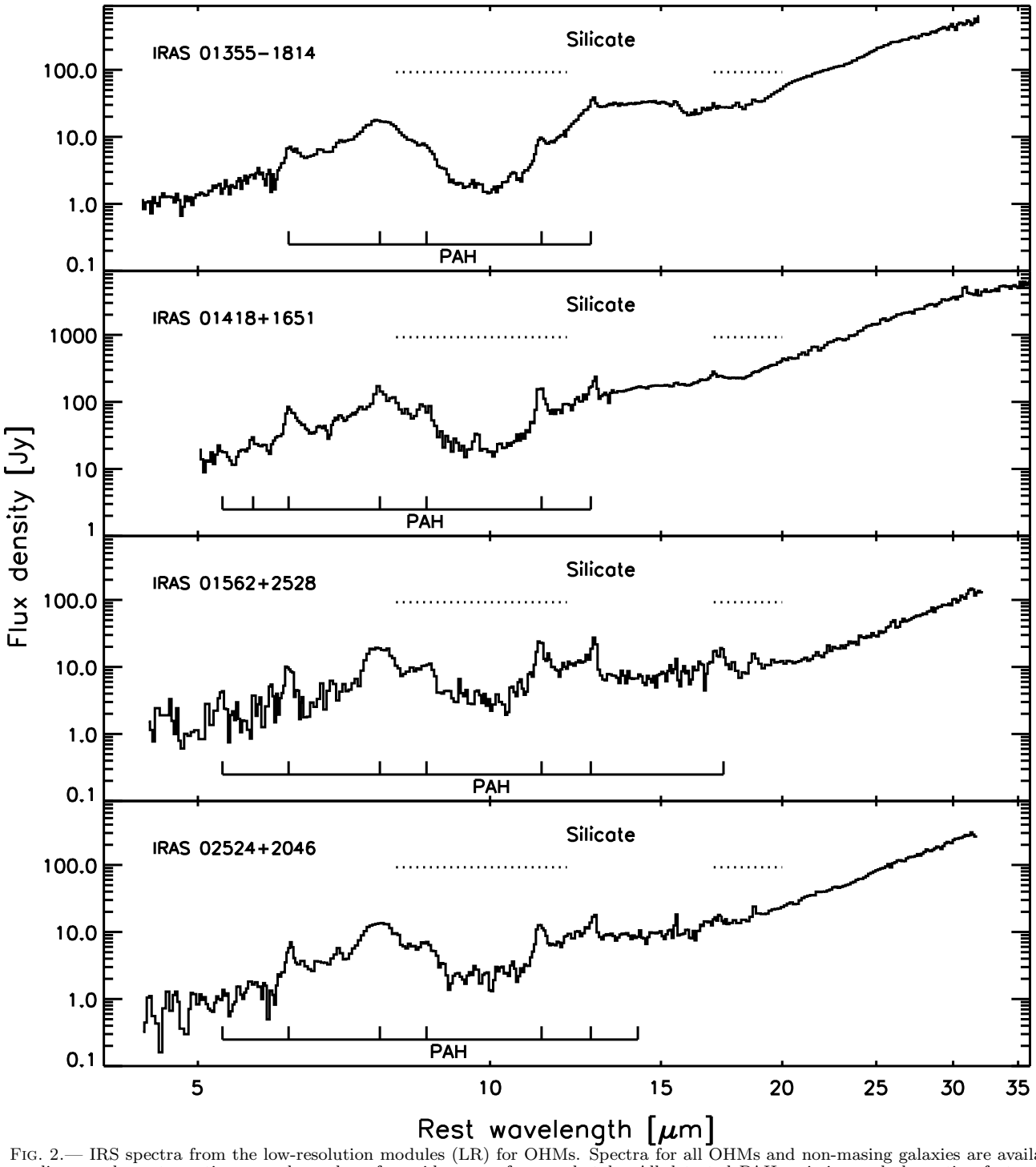

FIG. 2.— IRS spectra from the low-resolution modules (LR) for OHMs. Spectra for all OHMs and non-masing galaxies are available as an online supplement; portions are shown here for guidance on form and style. All detected PAH emission and absorption features from water ice and silicates are marked.

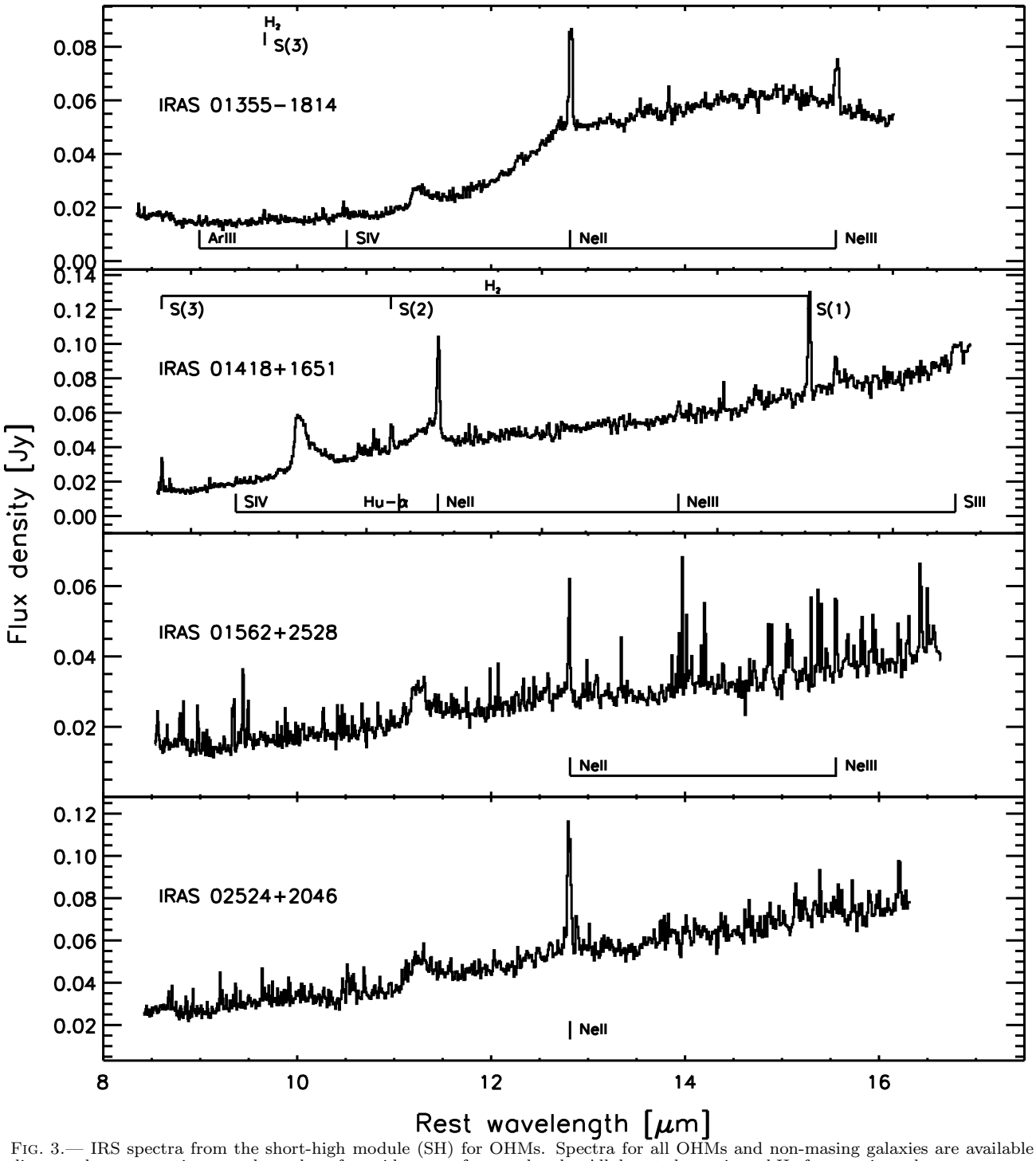

FIG. 3.— IRS spectra from the short-high module (SH) for OHMs. Spectra for all OHMs and non-masing galaxies are available as an online supplement; portions are shown here for guidance on form and style. All detected atomic and H_2 features in each spectra are marked.

TABLE 3
IRS PHOTOMETRY AND CONTINUUM MEASUREMENTS

Object	16 μm PU [mJy]	22 μm PU [mJy]	PU type	α_{15-6}	α_{30-20}	S/N
IRAS 01355−1814	...	45.5	DCS	2.8 ± 0.3	5.2 ± 0.8	75
IRAS 01418+1651	...	...	...	2.2 ± 0.3	5.2 ± 0.8	18
IRAS 01562+2528	6.1	13.0	SUR	1.8 ± 0.3	5.1 ± 0.8	11
IRAS 02524+2046	10.6	21.7	SUR	2.0 ± 0.4	5.7 ± 1.0	25
IRAS 03521+0028	25.6	...	DCS	2.3 ± 0.4	5.5 ± 0.8	63
IRAS 04121+0223	10.5	22.6	SUR	2.6 ± 0.1	5.9 ± 0.5	21
IRAS 04454−4838	...	...	...	2.7 ± 0.4	6.1 ± 0.9	37
IRAS 06487+2208	85.0	177.5	SUR	2.4 ± 0.2	3.6 ± 0.8	48
IRAS 07163+0817	12.3	28.8	SUR	2.5 ± 0.3	4.8 ± 1.0	26
IRAS 07572+0533	52.1	103.0	SUR	2.6 ± 0.3	3.0 ± 0.7	55
IRAS 08201+2801	61.8	74.3	SUR	2.2 ± 0.2	4.5 ± 0.7	37
IRAS 08449+2332	26.6	48.2	SUR	2.2 ± 0.2	4.4 ± 0.4	52
IRAS 08474+1813	9.5	28.7	SUR	2.2 ± 0.5	6.5 ± 0.6	30
IRAS 09039+0503	86.7	...	DCS	1.8 ± 0.5	5.5 ± 0.7	41
IRAS 09539+0857	...	...	...	2.2 ± 0.1	6.0 ± 0.3	36
IRAS 10035+2740	9.2	22.8	SUR	2.1 ± 0.2	6.0 ± 0.5	23
IRAS 10039−3338	...	...	...	-0.1 ± 0.1	5.4 ± 0.3	17
IRAS 10173+0828	...	...	...	2.6 ± 0.4	6.4 ± 1.0	48
IRAS 10339+1548	10.7	28.1	SUR	2.5 ± 0.3	5.1 ± 0.7	22
IRAS 10378+1109	...	114.8	DCS	2.0 ± 0.3	4.5 ± 0.7	35
IRAS 10485−1447	...	...	...	2.5 ± 0.3	4.8 ± 0.8	75
IRAS 11028+3130	4.8	13.0	SUR	2.4 ± 0.2	7.0 ± 0.6	26
IRAS 11180+1623	14.8	33.6	SUR	2.2 ± 0.3	5.6 ± 0.9	15
IRAS 11524+1058	8.2	14.8	SUR	1.5 ± 0.4	6.1 ± 0.8	20
IRAS 12018+1941	121.7	...	DCS	3.0 ± 0.3	2.9 ± 0.4	63
IRAS 12032+1707	...	73.9	DCS	2.2 ± 0.3	4.2 ± 0.7	42
IRAS 12112+0305	91.9	...	DCS	2.3 ± 0.3	5.3 ± 0.7	42
IRAS 12540+5708	...	...	...	1.6 ± 0.3	2.4 ± 0.7	30
IRAS 13218+0552	212.9	...	DCS	0.6 ± 0.3	2.4 ± 0.7	100
IRAS 13428+5608	...	...	...	1.9 ± 1.3	4.6 ± 0.6	12
IRAS 13451+1232	...	...	...	2.3 ± 0.4	1.9 ± 0.7	50
IRAS 14059+2000	12.2	26.3	SUR	1.1 ± 0.6	4.9 ± 0.8	20
IRAS 14070+0525	...	30.1	DCS	1.6 ± 0.3	5.6 ± 0.5	33
IRAS 14553+1245	28.7	61.2	SUR	2.0 ± 0.7	4.3 ± 0.7	22
IRAS 15327+2340	...	...	...	2.4 ± 0.2	5.5 ± 0.4	17
IRAS 16090−0139	71.4	...	DCS	1.3 ± 0.4	4.6 ± 0.6	59
IRAS 16255+2801	16.0	36.7	SUR	1.4 ± 0.3	4.7 ± 0.6	22
IRAS 16300+1558	...	35.0	DCS	1.7 ± 0.5	5.6 ± 0.9	31
IRAS 17207−0014	...	...	...	1.8 ± 0.6	6.2 ± 0.6	28
IRAS 18368+3549	26.6	49.8	SUR	1.7 ± 0.5	5.4 ± 0.8	29
IRAS 18588+3517	43.6	92.1	SUR	1.5 ± 0.3	4.8 ± 0.8	28
IRAS 20100−4156	86.7	...	DCS	1.9 ± 0.2	5.2 ± 0.7	73
IRAS 20286+1846	11.4	22.0	SUR	2.3 ± 0.3	5.8 ± 0.6	20
IRAS 21077+3358	31.1	62.1	SUR	2.8 ± 0.3	4.2 ± 0.6	52
IRAS 21272+2514	...	39.0	DCS	2.0 ± 0.3	5.0 ± 0.7	36
IRAS 22055+3024	54.5	132.4	SUR	2.7 ± 0.3	4.0 ± 0.7	30
IRAS 22116+0437	46.6	68.2	SUR	2.3 ± 0.5	4.5 ± 0.9	35
IRAS 22491−1808	87.5	...	DCS	2.8 ± 0.3	5.1 ± 0.6	28
IRAS 23028+0725	56.4	140.7	SUR	...	3.2 ± 0.7	25
IRAS 23233+0946	...	...	...	2.1 ± 0.3	4.7 ± 0.5	33
IRAS 23365+3604	...	...	...	2.5 ± 3.1	4.6 ± 0.5	15
IRAS 00163−1039	...	...	...	2.3 ± 0.4	2.1 ± 0.4	34
IRAS 01572+0009	...	...	...	1.8 ± 0.2	2.2 ± 0.3	81
IRAS 05083+7936	...	...	...	2.0 ± 0.4	2.8 ± 0.4	48
IRAS 06538+4628	...	...	...	2.9 ± 0.3	2.5 ± 0.4	37
IRAS 08559+1053	...	90.7	DCS	1.3 ± 0.1	2.8 ± 0.4	64
IRAS 09437+0317	...	...	...	1.7 ± 0.3	2.2 ± 0.4	19
IRAS 10565+2448	...	...	...	2.1 ± 0.4	3.2 ± 0.5	19
IRAS 11119+3257	...	...	...	1.2 ± 0.1	2.5 ± 0.3	79
IRAS 13349+2438	...	...	...	0.8 ± 0.1	0.1 ± 0.1	110
IRAS 15001+1433	...	135.3	DCS	1.9 ± 0.2	3.4 ± 0.5	58
IRAS 15206+3342	110.7	...	DCS	2.3 ± 0.4	2.6 ± 0.4	65
IRAS 20460+1925	...	...	...	...	1.1 ± 0.3	16
IRAS 23007+0836	...	...	...	1.7 ± 0.1	1.8 ± 0.4	19
IRAS 23394−0353	...	...	...	1.8 ± 0.3	2.9 ± 0.4	37
IRAS 23498+2423	46.5	...	DCS	1.0 ± 0.1	3.1 ± 0.4	87

NOTE. — Errors in the peakup (PU) fluxes are at the 15% level.

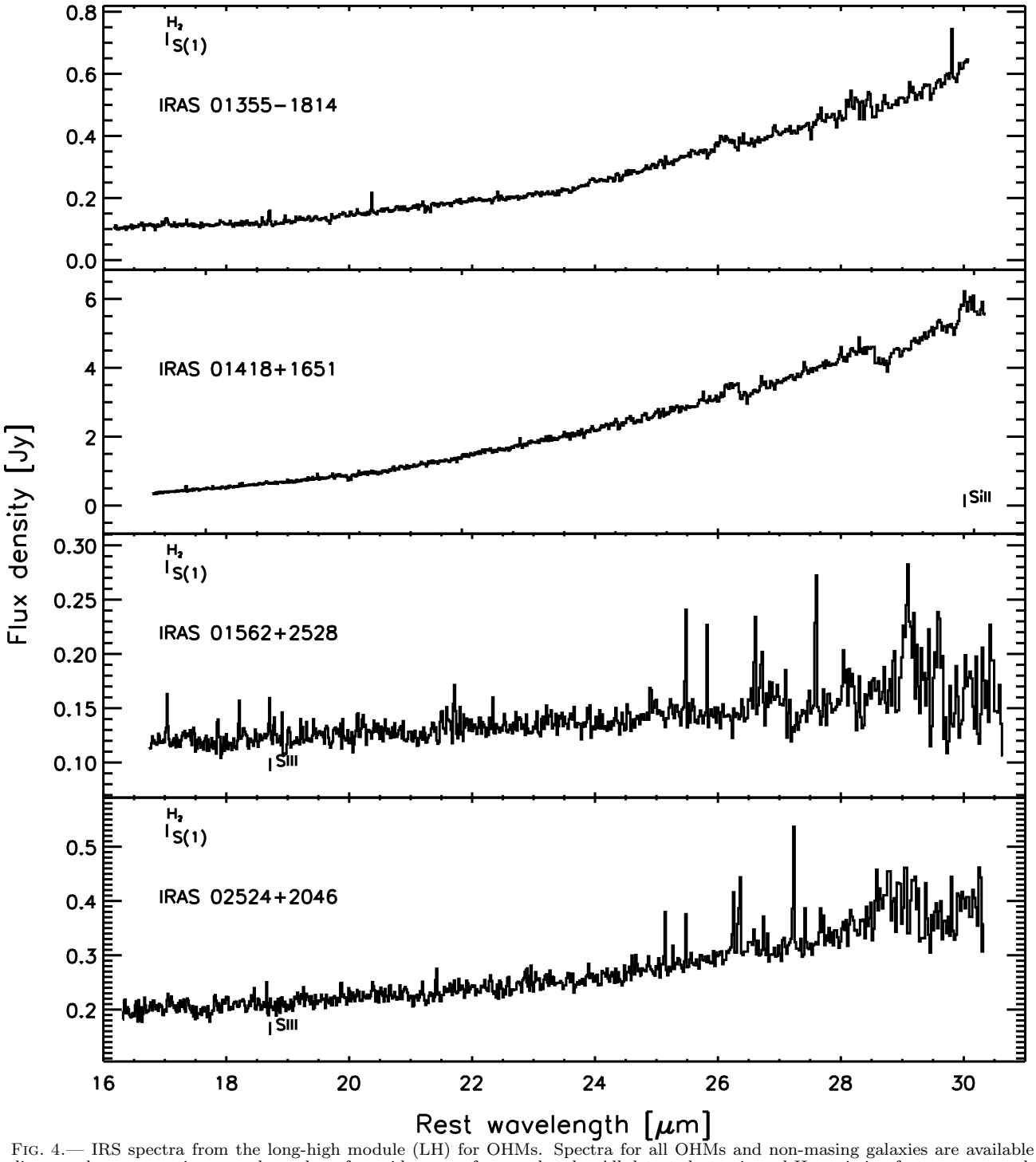

FIG. 4.— IRS spectra from the long-high module (LH) for OHMs. Spectra for all OHMs and non-masing galaxies are available as an online supplement; portions are shown here for guidance on form and style. All detected atomic and H_2 emission features are marked.

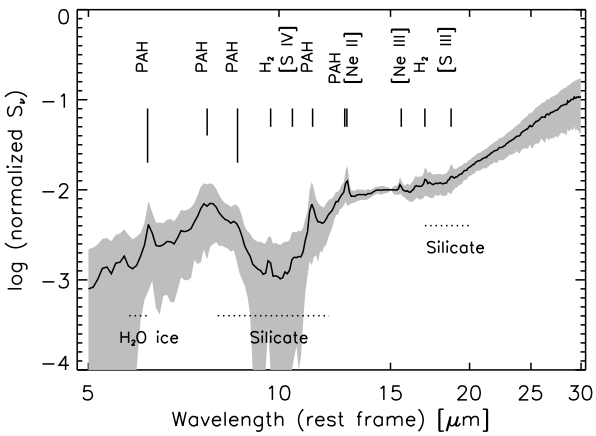

FIG. 5.— Low-resolution spectrum of all galaxies in our sample normalized at $S_\lambda = 15$ μm. The black spectrum is the composite template made from an error-weighted median of the individual galaxies; the grey shaded area shows the 1-σ envelope for each resolution element (exaggerated toward negative values in log space).

($\alpha_{30-20} = 7.0$); the galaxy shows moderate PAH and line emission features, but a flat continuum between 12 and 20 μm.

The non-masing galaxies have average spectral indices of $\alpha_{15-6} = 1.8 \pm 0.6$ and $\alpha_{30-20} = 2.5 \pm 0.9$. A full statistical analysis of the values for the two samples (particularly α_{30-20}) is presented in Paper II.

5.2. *Atomic emission lines*

We measured emission from atomic and molecular lines using the standard packages in the Spectroscopic Modeling Analysis and Reduction Tool (SMART) v6.2.4 (Higdon et al. 2004). A simple Gaussian is a good fit for virtually all high-resolution lines in the sample; in cases where lines are blended (such as the [Ne V]/[Cl II] and [O IV]/[Fe II] complexes), we used a multi-Gaussian fit centered at the redshifted rest wavelengths of the expected transitions. To compute upper limits for non-detections, we use the 3-σ noise measured from the surrounding continuum and a Gaussian shape with an FWHM estimated from detected lines. Accuracy for all measured line fluxes is on the order of $\sim 10\%$ (Tables 4 and 5).

The most common lines detected are the forbidden [Ne II] λ12.814 and [Ne III] λ15.555 transitions. [Ne II] is observed in nearly the entire sample, with detections in 50/51 OHMs and 14/15 non-masing galaxies. The only exceptions are the OHM IRAS 11028+3130 and the non-maser IRAS 20460+1925. [Ne III] is also common, detected in 43/51 OHMs and 14/15 non-masing galaxies. Other common lines are the [S III] λ18.713 (detected in $\sim 80\%$ of galaxies) and [S IV] λ10.511 ($\sim 50\%$). [Ar III] λ8.991 is detected in 15 OHMs and 5 non-masing galaxies, but the redshifted line is not visible in the SH module for archived objects at $z < 0.1$.

We detect "rarer" line transitions that appear in less than 15% of our sample, including [Ne V] λ14.322 and λ24.318, [Fe II] λ17.936 and λ25.988, and [O IV] λ25.890. IRAS 10339+1548 is the only galaxy in the sample with detections for all atomic transitions listed above. Eight galaxies also show the non-forbidden HI 7-6 transition (Humphreys-α) at 12.368 μm.

[S III]λ33.481 and [Si II]λ34.815 are commonly observed in ULIRGs for which the redshifted transitions appear within the red edge of the LH module. Farrah et al. (2007) detected [S III]λ33.481 in roughly half of all ULIRGs with $z < 0.06$, all of which show the stronger [S III]λ18.713 associated transition. For our sample, however, many galaxies have the lines redshifted beyond the range of the IRS; when visible, the lines lie at the far red edge of the 11$^{\rm th}$ order in the LH module, an area with high noise and decreased sensitivity with respect to neighboring orders.

For galaxies taken from the *Spitzer* archive, we compared our high-resolution measurements with those appearing in the sample of Farrah et al. (2007). The agreement between detected lines is good for nearly all objects; however, Farrah et al. (2007) report detections of [Ne V] in IRAS 11119+3257, [O IV] in IRAS 13451+1232, and H_2 S(0) and S(2) lines in IRAS 01572+0009 and IRAS 23498+2423 which we fail to confirm. Limits for the measured fluxes are given in Tables 4 and 5 and 6.

The IRS is designed to make accurate measurements of narrow atomic transitions in the SH and LH modules; however, several lines are also detected in the LR modules, most often the powerful neon, sulfur, and H_2 transitions. The only emission lines visible in the low-resolution modules without a corresponding detection in high-resolution are the H_2 S(7) line at 5.5 μm and the H_2 S(5)/[Ar II] complex near 6.7 μm; this is due to the SH low-wavelength cutoff at $\lambda_{rest} = 8.2 - 9.0$ μm, depending on the redshift of the galaxy. All other atomic emission features observed in the low-resolution modules have corresponding detections in high-resolution; furthermore, blending of narrow lines makes accurate measurements of flux difficult in the LR modules. For isolated lines with well-defined surrounding continuum, our fluxes are consistent for measurements in both low- and high-resolution.

We note the presence of two features which have no obvious identifications occurring in the LH spectra for multiple objects: one is an emission feature seen near 29 μm (a prominent example occurs for IRAS 17539+2935) and the second is an absorption feature near 30 μm. The two are often paired and are seen in $\sim 50\%$ of the galaxies observed. The *rest* wavelengths of the transitions, however, vary significantly from object to object (with a standard deviation of $\sigma_\lambda \simeq 0.7$ μm), while the *observed* wavelengths are nearly fixed ($\sigma_\lambda \lesssim 0.05$ μm). This implies that the features are either artifacts of the extraction process or that both the emission and absorption come from unidentified foreground features with little to no Doppler shift. Given that we see no evidence for these unidentified lines in any of the LR spectra (which should be detectable, given the high S/N for many of the features), we consider both to be spurious.

5.3. *Molecular hydrogen*

We detected multiple emission lines from the pure rotational series of molecular hydrogen in both OHMs and non-masing galaxies. At redshifts of $z \lesssim 0.1$, transitions from H_2 S(0) at 28.22 μm to H_2 S(3) at 9.67 μm are visible in the HR modules; in addition, the LR module is capable of detecting lines as far out as the S(7) tran-

TABLE 4
Atomic line fluxes for high-resolution spectra: 8 − 16 microns

Object λ_{rest} [μm]	[Ar III] 8.991	[S IV] 10.511	H I 7-6 12.368	[Ne II] 12.814	[Ne V] 14.322	[Cl II] 14.369	[Ne III] 15.555
IRAS 01355−1814	0.15	0.10	< 0.20	2.45	< 0.27	< 0.25	0.89
IRAS 01418+1651	–	0.15	0.13	4.17	< 0.46	< 0.29	0.41
IRAS 01562+2528	< 0.77	< 1.93	< 0.30	1.07	< 0.91	< 0.75	0.77
IRAS 02524+2046	< 0.63	< 1.01	< 0.36	2.39	< 0.68	< 0.56	< 0.97
IRAS 03521+0028	< 0.34	< 0.40	< 0.41	2.72	< 0.36	< 0.24	1.11
IRAS 04121+0223	0.35	< 0.84	< 0.41	1.81	< 1.01	< 0.99	< 0.87
IRAS 04454−4838	–	0.47	< 0.74	2.04	< 0.75	< 0.61	0.39
IRAS 06487+2208	1.71	1.78	< 0.81	11.75	< 1.44	< 1.19	9.45
IRAS 07163+0817	0.44	< 1.05	< 0.22	3.19	< 0.46	< 0.39	0.33
IRAS 07572+0533	< 1.69	< 0.87	< 0.40	1.74	< 0.79	< 0.65	< 0.89
IRAS 08201+2801	< 0.70	< 2.74	< 0.64	2.23	< 0.60	< 0.41	0.88
IRAS 08449+2332	< 0.94	< 0.71	< 0.64	3.60	< 2.03	< 1.64	1.57
IRAS 08474+1813	< 0.76	< 0.64	< 0.36	1.26	< 1.10	< 0.89	< 1.10
IRAS 09039+0503	0.11	< 0.27	< 0.85	3.68	< 0.46	< 0.38	1.17
IRAS 09539+0857	< 0.63	< 0.43	< 0.30	1.25	< 0.86	< 0.69	< 1.88
IRAS 10035+2740	< 0.89	< 0.75	< 0.48	1.82	< 0.42	< 0.31	0.57
IRAS 10039−3338	–	0.93	< 1.25	16.69	< 1.21	< 1.10	3.93
IRAS 10173+0828	–	< 0.29	< 0.34	1.71	< 0.33	< 0.32	0.46
IRAS 10339+1548	1.00	0.55	< 0.34	1.25	1.24	< 1.13	2.03
IRAS 10378+1109	0.34	< 0.25	< 0.35	3.95	< 0.61	< 0.63	0.68
IRAS 10485−1447	< 1.14	< 0.20	< 0.23	1.99	< 0.44	< 0.48	0.36
IRAS 11028+3130	< 1.06	< 0.70	< 0.28	< 0.63	< 0.44	< 0.38	< 0.74
IRAS 11180+1623	< 0.80	< 0.70	< 0.36	1.98	< 0.50	< 0.39	0.62
IRAS 11524+1058	< 0.78	< 0.56	< 0.35	7.82	< 0.43	< 0.37	< 0.77
IRAS 12018+1941	< 0.27	< 0.28	< 0.59	2.73	< 0.52	< 0.38	0.64
IRAS 12032+1707	< 1.33	0.13	< 0.48	4.98	1.39:	< 1.51	1.57
IRAS 12112+0305	–	0.43	< 0.88	13.06	< 0.76	< 0.55	3.37
IRAS 12540+5708	–	< 11.45	< 4.40	17.95	< 8.05	< 6.86	9.36
IRAS 13218+0552	< 0.66	< 0.54	< 0.46	0.84	< 0.71	< 1.23	< 1.24
IRAS 13428+5608	–	7.69	< 2.42	41.21	10.62	< 5.37	29.05
IRAS 13451+1232	0.57	1.57	< 0.70	4.71	0.71	< 0.88	4.73
IRAS 14059+2000	< 0.64	0.35	< 0.53	2.83	< 0.88	< 1.00	2.65
IRAS 14070+0525	< 0.19	< 0.18	< 0.27	1.33	< 0.42	< 0.33	2.01
IRAS 14553+1245	0.47	0.71	< 0.25	3.24	< 1.55	< 1.29	3.10
IRAS 15327+2340	–	< 0.79	< 3.60	61.13	< 6.29	< 5.29	6.89
IRAS 16090−0139	0.49	0.10	< 0.49	6.72	< 0.65	< 0.76	2.26
IRAS 16255+2801	0.18	0.20	< 0.27	1.73	< 0.82	< 0.68	1.18
IRAS 16300+1558	0.13	< 0.15	< 0.28	2.27	< 0.33	< 0.25	0.42
IRAS 17207−0014	–	0.40	< 2.12	38.84	< 0.93	< 0.69	8.42
IRAS 18368+3549	< 0.42	< 0.81	0.11	6.91	< 0.34	< 0.43	1.07
IRAS 18588+3517	0.57	0.37	0.24	5.12	< 0.40	< 0.43	1.87
IRAS 20100−4156	0.33	0.23	< 0.31	6.73	< 0.65	< 0.49	1.71
IRAS 20286+1846	< 0.56	< 0.50	< 0.27	1.67	< 0.72	< 0.65	0.37
IRAS 21077+3358	< 0.67	< 0.63	< 0.39	3.06	< 0.45	< 0.36	1.09
IRAS 21272+2514	< 0.18	< 0.16	0.16	2.29	< 0.31	< 0.22	0.35
IRAS 22055+3024	0.12	< 0.67	< 0.71	4.55	< 0.76	< 0.74	1.05
IRAS 22116+0437	< 0.47	< 0.73	< 0.37	2.25	< 0.82	< 0.68	1.33
IRAS 22491−1808	–	0.41	< 0.54	4.88	< 0.55	< 0.43	1.70
IRAS 23028+0725	< 0.55	< 0.61	< 0.39	1.81	< 0.90	< 0.72	1.04
IRAS 23233+0946	0.37	0.33	< 0.43	4.93	< 0.43	< 0.38	1.06
IRAS 23365+3604	–	< 0.36	< 0.51	8.51	< 0.63	< 0.52	1.12
IRAS 00163−1039	–	3.40	0.43	80.95	< 1.96	< 0.92	14.53
IRAS 01572+0009	0.73	3.06	< 0.72	6.15	5.51	< 3.23	10.34
IRAS 05083+7936	–	< 1.19	< 1.57	49.40	0.60	0.48	7.63
IRAS 06538+4628	–	0.80	1.09	47.39	0.69	< 1.16	6.07
IRAS 08559+1053	< 0.37	0.56	< 0.43	8.38	0.51	0.35	1.87
IRAS 09437+0317	–	< 1.04	< 0.61	8.74	< 0.64	< 0.51	1.22
IRAS 10565+2448	–	< 0.76	< 1.34	57.60	< 1.29	0.67	7.65
IRAS 11119+3257	< 0.83	0.31	< 0.78	2.19	< 0.71	< 0.58	1.89
IRAS 13349+2438	2.76	1.66	< 0.45	1.43	0.81	< 0.99	3.50
IRAS 15001+1433	0.39	0.28	< 0.30	6.61	1.08	< 0.98	2.62
IRAS 15206+3342	2.01	3.82	0.23	10.96	< 0.34	< 0.41	19.87
IRAS 20460+1925	< 0.39	< 0.66	< 0.42	< 0.44	< 0.60	< 0.51	< 0.69
IRAS 23007+0836	–	8.67	< 1.84	179.04	8.36	< 4.23	33.69
IRAS 23394−0353	–	0.72	0.57	46.75	< 1.45	< 1.08	7.71
IRAS 23498+2423	0.23	1.27	< 0.23	3.10	0.92	< 0.91	7.79

Note. — Line fluxes are given in 10^{-21} W cm^{-2}. – indicates that the redshifted line wavelength lay outside the range of the IRS.

TABLE 5
Atomic line fluxes for high-resolution spectra: 17 − 35 microns

Object	[Fe II]	[S III]	[Ne V]	[O IV]	[Fe II]	[S III]	[Si II]
λ_{rest} [μm]	17.936	18.713	24.318	25.890	25.988	33.481	34.815
IRAS 01355−1814	< 0.51	< 1.52	< 0.78	< 1.28	< 0.82	–	–
IRAS 01418+1651	< 0.67	0.94	< 3.84	< 3.52	< 4.05	< 24.62	19.43
IRAS 01562+2528	< 0.77	0.67	< 0.73	< 2.06	< 1.29	–	–
IRAS 02524+2046	< 1.11	0.47	< 1.04	< 0.96	< 0.59	–	–
IRAS 03521+0028	1.70	1.18	< 1.02	< 0.93	< 0.59	–	–
IRAS 04121+0223	< 0.92	0.93	< 1.06	0.97	< 1.34	–	–
IRAS 04454−4838	< 0.27	< 1.00	< 7.75	< 9.59	< 6.29	0.90	< 87.49
IRAS 06487+2208	< 0.87	4.89	< 1.36	0.48	1.31	–	–
IRAS 07163+0817	< 1.04	0.81	< 1.73	< 0.78	< 0.71	–	–
IRAS 07572+0533	< 0.61	< 1.15	< 1.37	< 1.53	< 1.03	–	–
IRAS 08201+2801	< 0.84	0.41	< 0.50	< 0.66	< 0.50	–	–
IRAS 08449+2332	< 0.60	1.62	< 0.73	< 0.69	< 0.40	–	–
IRAS 08474+1813	< 1.09	0.86	< 1.27	< 3.04	< 1.86	–	–
IRAS 09039+0503	< 0.85	0.88	< 0.55	< 1.11	0.48	–	–
IRAS 09539+0857	< 1.82	< 1.02	< 1.41	< 2.05	< 1.36	–	–
IRAS 10035+2740	< 0.97	0.78	< 0.95	< 2.11	< 1.37	–	–
IRAS 10039−3338	< 0.81	6.57	< 14.49	< 11.09	< 7.54	< 10.49	101.40
IRAS 10173+0828	< 0.42	< 1.36	< 1.33	< 2.42	< 1.61	2.55	81.70
IRAS 10339+1548	0.49	1.17	0.52	2.85	0.89	–	–
IRAS 10378+1109	< 0.95	1.82	< 0.87	< 1.99	< 1.30	–	–
IRAS 10485−1447	< 0.87	< 1.08	< 0.91	< 1.08	< 0.66	–	–
IRAS 11028+3130	< 0.47	< 0.71	< 3.07	< 4.45	< 3.14	–	–
IRAS 11180+1623	< 0.71	0.89	< 0.85	< 1.00	< 0.69	–	–
IRAS 11524+1058	< 0.52	< 1.61	< 1.49	< 0.93	< 0.70	–	–
IRAS 12018+1941	< 1.01	< 1.32	< 1.22	< 1.71	< 1.30	–	–
IRAS 12032+1707	< 1.22	1.18	0.66	< 1.50	< 1.00	–	–
IRAS 12112+0305	0.68	4.32	< 1.50	< 7.56	< 4.65	8.77	–
IRAS 12540+5708	< 4.40	< 5.05	< 22.99	< 18.84	< 14.43	< 49.65	< 163.66
IRAS 13218+0552	< 0.78	< 2.27	< 1.85	< 2.93	< 1.76	–	–
IRAS 13428+5608	< 1.32	16.67	9.28	75.13	< 29.79	28.14	< 134.61
IRAS 13451+1232	< 1.19	1.15	< 2.50	< 5.17	< 1.85	–	–
IRAS 14059+2000	< 0.97	1.68	< 1.04	< 1.70	< 1.11	–	–
IRAS 14070+0525	< 0.53	< 0.77	< 1.25	< 1.98	< 1.37	–	–
IRAS 14553+1245	< 0.89	1.58	< 0.89	< 2.38	< 1.49	–	–
IRAS 15327+2340	< 1.04	5.19	< 24.96	< 24.33	< 15.22	< 151.68	< 202.18
IRAS 16090−0139	1.03	3.07	< 3.95	1.12	< 2.23	–	–
IRAS 16255+2801	< 5.36	1.54	< 12.06	< 7.16	< 4.83	–	–
IRAS 16300+1558	< 1.20	0.50	< 1.23	< 0.88	< 0.70	–	–
IRAS 17207−0014	< 0.51	6.39	< 6.40	< 11.27	< 7.70	12.24	46.91
IRAS 18368+3549	< 0.49	1.18	< 1.07	< 0.91	< 0.59	–	–
IRAS 18588+3517	< 3.75	7.96	< 4.91	< 4.13	< 4.05	–	–
IRAS 20100−4156	< 0.69	2.86	< 3.58	1.20	1.34	–	–
IRAS 20286+1846	< 0.30	0.44	< 0.58	< 0.73	< 0.70	–	–
IRAS 21077+3358	< 0.50	0.77	< 0.80	< 0.60	< 0.47	–	–
IRAS 21272+2514	< 0.21	0.45	< 0.50	< 0.68	< 0.46	–	–
IRAS 22055+3024	< 0.51	1.04	< 2.12	< 2.30	< 1.34	–	–
IRAS 22116+0437	< 1.07	1.04	< 2.16	< 2.54	< 2.35	–	–
IRAS 22491−1808	< 0.72	1.86	< 3.40	< 7.11	< 3.35	13.72	–
IRAS 23028+0725	< 1.05	< 1.15	< 1.72	< 2.70	< 1.72	–	–
IRAS 23233+0946	< 0.89	3.13	< 1.06	1.20	0.66	–	–
IRAS 23365+3604	< 0.44	4.29	< 4.74	< 11.96	< 7.97	6.81	–
IRAS 00163−1039	< 1.70	30.85	< 7.59	1.42	3.35	34.70	73.84
IRAS 01572+0009	< 0.89	1.66	4.76	9.82	< 6.12	–	–
IRAS 05083+7936	< 1.19	18.67	< 1.89	1.28	1.33	28.00	71.27
IRAS 06538+4628	1.17	19.11	< 2.33	< 6.97	2.70	37.60	57.37
IRAS 08559+1053	< 0.93	1.35	< 1.34	2.54	0.45	–	–
IRAS 09437+0317	< 0.70	3.33	< 0.99	0.47	0.68	9.45	23.27
IRAS 10565+2448	< 1.02	12.42	< 3.07	< 5.13	< 2.35	20.89	51.37
IRAS 11119+3257	< 2.30	< 1.75	< 2.40	< 3.08	< 1.95	–	–
IRAS 13349+2438	< 4.54	1.68	3.46	7.28	< 5.11	–	–
IRAS 15001+1433	< 0.78	2.36	0.67	1.21	0.56	–	–
IRAS 15206+3342	< 1.03	8.58	1.36	0.74	1.21	–	–
IRAS 20460+1925	< 0.72	< 0.79	< 3.68	1.95	< 1.01	–	–
IRAS 23007+0836	< 3.28	70.16	15.51	30.98	9.47	97.56	188.36
IRAS 23394−0353	< 1.10	17.16	< 1.92	1.27	2.43	44.29	53.48
IRAS 23498+2423	< 0.55	1.13	1.26	4.61	< 3.77	–	–

Note. — Line fluxes are given in 10^{-21} W cm^{-2}. – indicates that the redshifted line wavelength lay outside the range of the IRS.

sition at 5.51 μm. In each case, the line number [*eg*, 0 for H_2 S(0)] indicates the rotational quantum number of the lower state ($J = 2 \rightarrow 0$) for the quadrupole S-branch transition. $\Delta J = 2$ results in two separate branches: ortho (parallel nuclear spin, odd J) and para (anti-parallel nuclear spin, even J).

We detected at least one H_2 line in 49/51 OHMs and 13/15 non-masing galaxies, with S(1) seen in all objects for which at least one molecular hydrogen transition is reported. The higher-order S(2) and S(3) lines are seen in roughly 2/3 of the sample, while the para ground state S(0) transition is detected in only $\sim 15\%$ of the sample. Our line detection rate is consistent with results from the SINGS galaxies examined in Roussel et al. (2007) and the ULIRG sample of Higdon et al. (2006). Lower detection rates of S(0) and S(2) are likely due to a combination of the intrinsic ortho-para ratio as well as rising continuum levels near 28 μm that can obscure weak line emission by S(0). Higdon et al. (2006) find that the S(2)/S(3) ratios are consistent with no significant differential extinction for the two lines, which is supported by numerous detections in our sample of S(3) line emission superimposed on optically deep silicate absorption near 9.7 μm. We thus applied no extinction or reddening corrections to the line fluxes (Table 6).

We did not detect the S(6) line in any galaxy, while S(4) showed a single detection in IRAS 16300+1558. Since these lines are excited by hotter gas ($T \sim 1000$ K), they are typically weaker than the lower states which probe the larger reservoir of cool gas. In addition, both lines are only visible in the low-resolution modules at $z \sim 0.1$. This means that deblending is a significant issue, since both lines lie near broad PAH emission complexes. 11 OHMs and one non-masing galaxy show the unresolved S(7) ortho line at 5.51 μm in the SL module.

Measurement of the S(5) line presents a particular problem due to its location in a crowded section of the spectra. Its rest wavelength of 6.91 μm lies near the [Ar II] feature at 6.99 μm; in addition, both features are bracketed by possible hydrocarbon absorption at 6.85 and 7.25 μm. This not only creates difficulties in establishing a reliable continuum, but also in deblending the [Ar II] and the S(5) emission (see §5.5.2). Emission in the [Ar II]/H_2 S(5) complex is seen in more than half of our sample, however, and so we present measurements for the *entire* feature, including blended emission from both lines. We caution that these fluxes should be viewed as upper limits for either [Ar II] or H_2 S(5) emission, since the SL module does not have sufficient resolution to separate the two features.

For galaxies in which multiple H_2 lines are observed, we fit excitation temperatures (T_{ex}) to the molecular gas following the methods of Rigopoulou et al. (2002) and Higdon et al. (2006). We assume that the emission is optically thin (so that the lines are unsaturated), populations are in local thermodynamic equilibrium (LTE), and that the sources are unresolved in the *Spitzer* beam. The luminosity of a molecular emission line for the transition from $(J+2) \rightarrow J$ is then $L_J = A_J \times \Delta E_J \times N_{J+2}$, where A_J is the Einstein-A coefficient, ΔE_J is the energy of the transition, and N_{J+2} is the number of molecules in the $J+2$ state. The partition function for a given symmetry branch is:

$$Z_{J_{o/p}} = \sum_{J_{o/p}} g_J \; exp[-E_J/kT_{ex}] \qquad (2)$$

where T_{ex} is the excitation temperature and we sum only over a single symmetry branch (ortho or para). The statistical weights are $g_J = (2J+1) \times J_s$, where $J_s = 1$ for the para branch (even J) and $J_s = 3$ for ortho (odd J).

Assuming that the lines are in LTE, the ratio of level populations follows a Boltzmann distribution such that $N_J \propto \; g_J \; exp[-E_J/k \; T_{ex}]$. The inverse slope of the best-fit line of an excitation diagram yields T_{ex} - Figure 6 shows examples of temperature fits for our data. The total warm H_2 mass can be then calculated from T_{ex} and the flux (F_J) from any transition as:

$$M_{tot} = m_{H_2} \times \phi_{o/p} \times \frac{(4\pi D_L^2) F_J Z_{J_{o/p}}}{A_J \Delta E_J g_J \; exp[-E_J/kT_{ex}]} \qquad (3)$$

where $\phi_{o/p}$ is a numerical factor accounting for the ortho-to-para ratio (assumed to be 3:1), m_{H_2} is the mass of the hydrogen molecule, and D_L is the luminosity distance.

For cases where the S(7) line was detected, a single excitation temperature gives a poor fit to the full set of transitions. In these cases, we first fit T_{ex} between S(3) and S(7), measuring hotter gas. We then subtracted this component from the S(0) to S(3) fluxes, and fit a second T_{ex} to the warm gas component. This decreased the mean warm T_{ex} by ~ 20 K, with a negligible effect on the gas mass. We calculated the warm H_2 mass using the flux in the S(1) transition and the hot gas mass using the S(3) flux (Table 6).

Both Higdon et al. (2006) and Roussel et al. (2007) suggest that the H_2 emission arises from far-ultraviolet photons from massive stars powering photodissociation regions (PDRs). Detections of the H_2 S(3) transition in nearly all objects implies that the silicate absorption at 9.7 μm must be partially background to the warm molecular gas seen in emission. Since the dust is very optically thick in almost all ULIRGs, this means that at least some molecular gas (and possibly other atomic transitions) actually come from superficial layers at the edge of the merging system. Given that the OHM is typically formed within the central kiloparsec of the host galaxy, a link between the observed warm H_2 gas and the OHM is uncertain.

11 objects in the OHM sample and 2 non-masing galaxies have CO detections published in the literature (Solomon et al. 1997; Gao & Solomon 2004a). The beam width used for CO observations is several times that of the HR slits; since most ULIRGs are unresolved in the *Spitzer* beam, we consider the gas mass estimates to be comparable. The cold gas masses derived using a ULIRG-calibrated M_{H_2}/L_{CO} ratio of $\sim 1.4 M_\odot$/(K km s^{-1} pc^2) give a warm gas mass fraction for the OHMs ranging from $0.04 - 0.8\%$, with the gas fraction of the non-masing galaxies lying in a similar range ($0.06-0.1\%$). This is comparable to warm gas fractions in ULIRGs from Higdon et al. (2006), implying that the mid-IR H_2 lines probe only a small amount of the total gas mass in these galaxies. The bulk of the remaining portion is likely cold gas without sufficient energy to excite rotational transitions in the mid-IR.

TABLE 6
MOLECULAR H_2 GAS PROPERTIES

Object	H_2 S(7)	H_2 S(5)	H_2 S(4)	H_2 S(3)	H_2 S(2)	H_2 S(1)	H_2 S(0)	T_{warm}	T_{hot}	M_{warm}	M_{hot}
λ_{rest} [μm]	5.51 μm	6.91 μm	8.03 μm	9.67 μm	12.28 μm	17.04 μm	28.22 μm	[K]	[K]	[10^7 $M_\odot$]	[10^7 $M_\odot$]
IRAS 01355−1814	< 1.52	< 3.25	–	0.22	0.63	1.13	< 1.63	262		4.74	
IRAS 01418+1651	< 5.29	6.96:	–	1.16	0.94	2.15	< 5.40	320		0.14	
IRAS 01562+2528	< 3.25	< 7.06	–	< 0.52	< 0.39	0.94	< 0.92				
IRAS 02524+2046	< 1.52	0.88:	–	< 2.51	< 0.46	0.88	< 1.03				
IRAS 03521+0028	< 2.89	0.58:	–	0.63	0.47	1.69	< 0.55	292		4.24	
IRAS 04121+0223	< 3.54	1.03:	–	< 1.62	< 0.43	< 0.73	< 1.06				
IRAS 04454−4838	< 3.31	< 13.24	–	1.04	1.27	3.05	0.76	222		0.82	
IRAS 06487+2208	< 5.99	0.97:	–	2.10	1.02	1.80	< 1.52	381		4.13	
IRAS 07163+0817	< 1.84	< 4.58	–	< 0.77	0.04	0.47	1.68	110		0.60	
IRAS 07572+0533	< 1.03	< 2.62	–	< 0.90	< 0.50	< 0.99	< 3.41				
IRAS 08201+2801	< 3.41	< 10.84	–	0.28	< 0.90	0.56	< 0.91	313		1.79	
IRAS 08449+2332	< 3.67	1.22:	–	0.63	0.33	1.36	< 0.70	301		3.48	
IRAS 08474+1813	< 1.07	0.61:	–	0.75	< 0.46	0.27	< 1.33	493		0.68	
IRAS 09039+0503	1.13	2.69:	–	2.21	1.46	2.91	1.27	198	978	4.88	0.42
IRAS 09539+0857	< 2.40	< 6.29	–	0.53	0.26	1.07	< 0.95	308		1.93	
IRAS 10035+2740	< 0.98	0.81:	–	0.70	< 0.63	1.06	< 2.31	334		3.29	
IRAS 10039−3338	< 28.84	< 46.95	–	3.27	1.71	3.95	< 7.46	348		0.46	
IRAS 10173+0828	< 5.73	3.00:	–	0.58	0.49	1.38	< 1.67	302		0.33	
IRAS 10339+1548	< 1.09	< 2.88	–	< 0.58	< 0.42	0.42	< 1.94				
IRAS 10378+1109	0.53	1.42:	–	1.82	0.55	2.25	< 0.61	315	876	4.59	0.46
IRAS 10485−1447	0.52	< 5.57	–	0.18	0.14	0.28	< 0.76	307	1540	0.55	0.03
IRAS 11028+3130	< 0.44	< 1.83	–	< 0.61	< 0.36	0.39	< 1.75				
IRAS 11180+1623	< 2.25	0.51:	–	0.39	0.61	1.06	< 1.88	302		3.32	
IRAS 11524+1058	< 1.99	< 4.35	–	< 0.43	< 0.42	0.66	< 2.14				
IRAS 12018+1941	< 3.27	< 8.84	–	0.47	0.36	1.28	2.21	165		4.10	
IRAS 12032+1707	< 2.78	4.93:	< 0.27	0.81	0.58	1.61	< 3.34	312		9.24	
IRAS 12112+0305	7.03	5.89:	–	1.87	1.66	3.71	1.30	195	1680	2.01	0.08
IRAS 12540+5708	< 32.27	< 49.24	–	2.42	3.21	6.23	< 17.62	301		1.07	
IRAS 13218+0552	< 4.32	< 7.55	–	0.32	0.42	0.97	< 2.91	292		4.83	
IRAS 13428+5608	< 13.14	8.96:	–	7.77	4.83	8.63	< 9.82	360		1.19	
IRAS 13451+1232	< 8.46	3.26:	–	1.65	1.10	2.61	< 0.79	329		4.18	
IRAS 14059+2000	0.91	1.55:	–	2.12	0.73	2.36	< 0.88	319	944	3.90	0.40
IRAS 14070+0525	< 2.54	< 5.85	< 0.41	0.28	0.22	1.30	< 0.85	260		11.42	
IRAS 14553+1245	0.32	< 9.92	–	0.92	0.19	1.05	< 0.82	317	906	1.76	0.19
IRAS 15327+2340	22.70	41.6:	–	< 0.56	7.66	13.68	14.53	159		0.42	
IRAS 16090−0139	1.20	< 15.12	–	1.10	< 0.28	2.12	< 2.93	299	1160	4.09	0.20
IRAS 16255+2801	< 1.82	0.21:	–	< 0.59	0.28	0.55	< 4.18	348		1.07	
IRAS 16300+1558	< 1.77	< 5.63	0.31	0.56	0.42	1.58	< 1.31	287		11.33	
IRAS 17207−0014	6.12	10.2:	–	4.56	4.44	7.51	< 3.60	311	1230	1.30	0.07
IRAS 18368+3549	< 6.98	4.22:	–	1.11	0.70	1.38	< 0.81	349		1.95	
IRAS 18588+3517	< 7.44	< 15.54	–	0.92	0.76	1.61	< 5.12	324		1.89	
IRAS 20100−4156	< 9.04	< 15.77	–	0.78	0.35	0.92	0.94	195		1.61	
IRAS 20286+1846	< 1.74	0.35:	–	< 0.78	0.30	0.92	< 0.51	282		1.80	
IRAS 21077+3358	< 2.13	1.59:	–	0.67	0.34	1.16	< 1.29	319		4.05	
IRAS 21272+2514	0.39	0.51:	–	0.36	0.28	0.91	< 0.46	287	1160	2.22	0.09
IRAS 22055+3024	0.65	2.52:	–	1.30	1.09	1.61	< 1.39	320	976	2.72	0.24
IRAS 22116+0437	< 2.45	< 6.21	–	0.74	0.64	1.09	< 1.82	340		4.70	
IRAS 22491−1808	< 7.01	< 14.81	–	0.76	0.92	2.10	< 8.22	298		1.23	
IRAS 23028+0725	–	–	–	0.48	0.45	0.77	< 1.67	333		1.86	
IRAS 23233+0946	< 3.20	1.60:	–	1.03	0.80	1.47	< 0.73	340		2.53	
IRAS 23365+3604	< 7.02	6.98:	–	1.26	0.73	2.14	< 5.75	321		0.84	
IRAS 00163−1039	< 9.00	24.46:	–	2.79	2.87	5.13	< 2.63	326		0.32	
IRAS 01572+0009	2.15	1.21:	–	0.60	< 0.71	2.15	< 1.36	268	1650	6.26	0.15
IRAS 05083+7936	< 8.11	27.31:	–	2.34	2.73	3.59	< 2.75	341		0.99	
IRAS 06538+4628	< 3.69	14.56:	–	< 0.63	3.28	8.86	2.63	189		0.38	
IRAS 08559+1053	< 5.91	1.76:	–	0.72	0.64	1.83	< 0.74	298		4.44	
IRAS 09437+0317	< 9.39	22.60:	–	< 0.36	0.68	2.68	2.20	153		0.11	
IRAS 10565+2448	< 12.33	32.87:	–	3.34	1.95	5.73	< 3.77	320		1.06	
IRAS 11119+3257	< 6.58	< 7.87	–	0.42	< 1.02	2.47	< 2.23	256		10.21	
IRAS 13349+2438	< 23.79	< 20.52	–	< 1.67	< 0.83	< 1.05	< 1.62				
IRAS 15001+1433	< 4.21	1.72:	–	0.44	0.24	1.25	< 0.84	283		3.72	
IRAS 15206+3342	< 8.31	1.61:	–	0.65	0.46	0.94	1.02	196		1.54	
IRAS 20460+1925	–	–	–	< 0.48	< 0.43	< 0.88	< 4.24				
IRAS 23007+0836	< 23.20	77.35:	–	< 3.53	6.30	12.90	< 6.28	342		0.27	
IRAS 23394−0353	< 14.60	32.52:	–	3.15	2.44	5.24	1.79	226		0.23	
IRAS 23498+2423	< 1.25	0.49:	–	0.34	< 0.29	0.89	< 1.50	298		4.66	

NOTE. — Line fluxes are given in 10^{-21} W cm^{-2}. – indicates that the redshifted line lay outside of the IRS spectral range. Fluxes for H_2 S(7) and S(5) are measured in the SL module; all other lines are measured in the SH and LH modules. S(5) lines are tentative upper limits (indicated by a :) due to possible blending with [Ar II] at 6.99 μm; see §5.3.

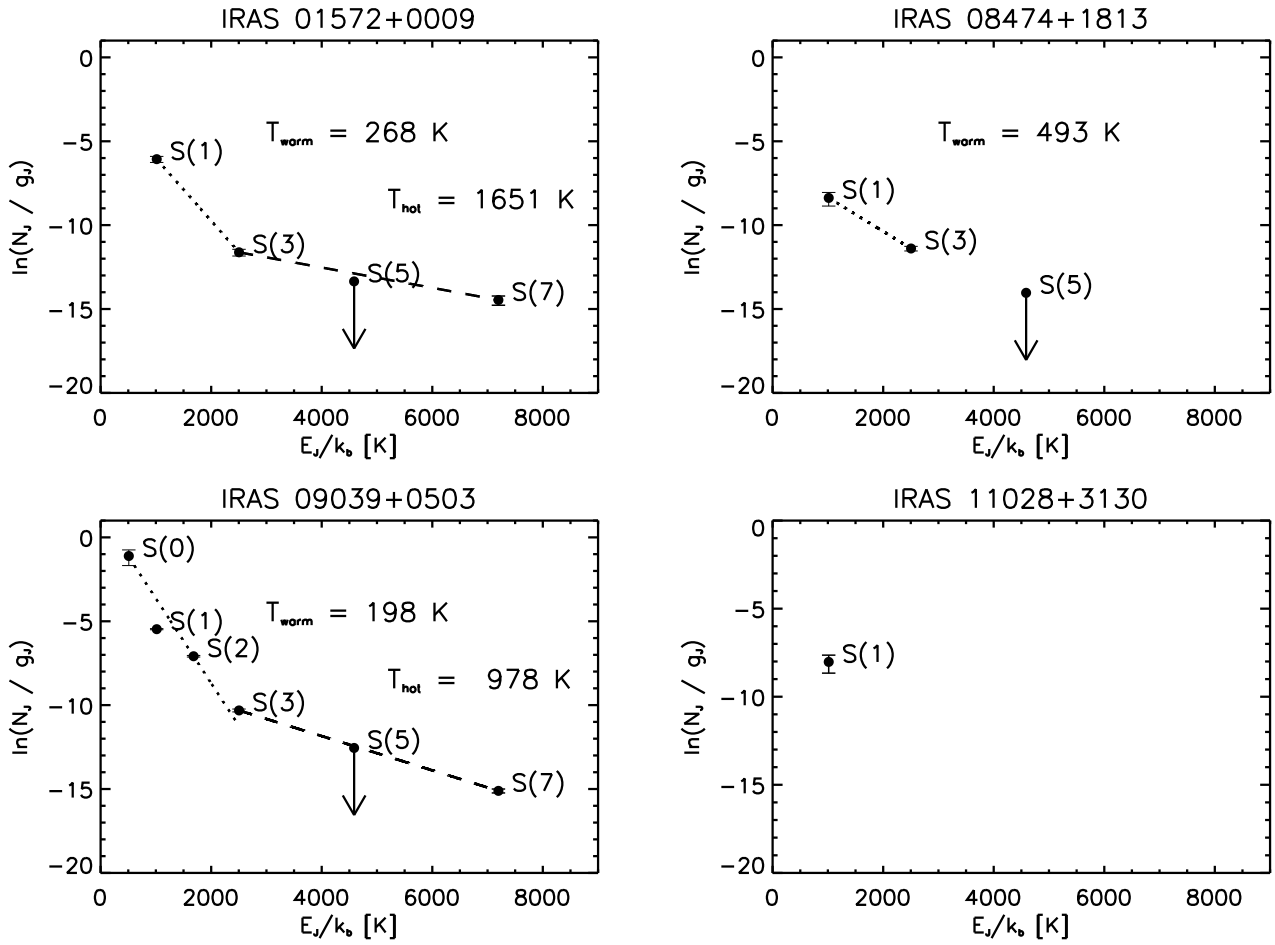

FIG. 6.— Example H_2 excitation diagrams for both non-masing (IRAS 01572+0009) and OHM galaxies (all others). Two galaxies (*left*) are fit with both warm and hot excitation temperatures; IRAS 08474+1813 fits only a warm component since the higher J lines are not detected. IRAS 11028+3130 shows an example of a galaxy with only a single H_2 detection (for which no T_{ex} can be determined). Dotted lines are fit to the warm gas for all detections from S(0) to S(3); dashed lines are fit to the hotter gas using detections of S(3), S(4) and S(7). The S(5) line is always an upper limit due to possible blending from [Ar II] and is not used in the temperature fits.

5.4. *PAH emission*

In addition to the atomic and simple molecular emission lines, we also observed multiple features attributed to polycyclic aromatic hydrocarbons (PAHs); the broad-line emission comes from vibrational modes of C-C and C-H bonds (Draine 2003). PAH features are ubiquitous in the mid-IR emission of starburst galaxies and ULIRGs (Lutz et al. 1998; Genzel et al. 1998; Sturm et al. 2000; Peeters et al. 2004; Desai et al. 2007; Imanishi et al. 2007), and dominate the low-resolution spectra of most galaxies in our sample. Multiple PAH features are seen for all OHMs, encompassing galaxies with very wide ranges in continuum shape and line emission. We detect strong PAH transitions centered at 6.2, 7.7, 8.6, 11.3, and 12.7 μm, several of which are also visible in the high-resolution spectra. Weaker emission features at 13.5, 14.2, 16.4, 17.1, and 17.4 μm are also visible in many galaxies.

We measured the PAH emission via two methods: the first defines a local continuum around the PAH feature using a spline fit, and then integrates the total flux after baseline subtraction. The default continuum pivots are located at 5.15, 5.55, 5.95, 6.55, and 7.10 μm for the 6.2 μm feature, and at 10.1, 10.9, 11.8, and 12.4 μm for the 11.3 μm feature. These are shifted slightly for each object to avoid both broad absorption features (including water ice and hydrocarbons) and narrow atomic emission lines. We quantify the emission from the two cleanest PAH features appearing in our spectra: the 6.2 and 11.3 μm complexes (Table 7).

A second method uses PAHFIT (Smith et al. 2007), a public IDL package, to fit global mid-IR spectral templates and simultaneously measure the relative effects of overlapping features. The routine decomposes the low-resolution IRS spectra into emission from stellar continuum, dust features (including PAHs), atomic and molecular lines, and blackbodies from thermally heated dust at a variety of temperatures; this is simultaneously fit with an extinction curve including silicate features at 9.7 and 18 μm. Due to the large number of parameters being fit, however, even strong features may overlap sufficiently to affect the accuracy of the fit (Spoon et al. 2002); in addition, PAHFIT does not fit for several features commonly found in ULIRGs, such as absorption features from ice, hydrocarbons, and gas-phase molecules.

PAHFIT fits the dust emission features (including PAHs) with a Drude profile, which has the form:

$$I_\lambda[\lambda] = \frac{b\gamma^2}{(\lambda/\lambda_c - \lambda_c/\lambda)^2 + \gamma^2}, \tag{4}$$

where λ_c is the central wavelength, γ is the fractional FWHM, and b is the (peak) central intensity. The Drude profile is typically broader than a Gaussian, with significant amounts of power in the extended wings. Several dust emission features (*eg*, the 7.7 and 12.7 μm PAHs) require more than one component for a reasonable fit. PAHFIT returned positive detections for both the 6.2 and 11.3 μm PAH features for nearly all galaxies; the fit for OHM IRAS 07572+0533 showed no emission at 6.2 μm, while the fits to OHM IRAS 13218+0552 and the non-masing galaxy IRAS 13349+2438 show no emission in either dust feature.

We compared the flux measured in the 6.2 and 11.3 μm PAH features from our baseline-subtracted spline fits to the PAHFIT values; results from PAHFIT are consistently higher than those from the spline fit, indicating significant mixing between the PAH emission and what was previously designated as "continuum" (Figure 7). Fluxes of the 6.2 μm complex measured with PAHFIT are a factor of $\sim 3-4$ greater than the spline-fit fluxes, while the 11.3 μm feature is an average of $\sim 2-3$ times larger. The relative strengths of the two features are consistent using both methods; the mean value of the (6.2 μm PAH/11.3 μm PAH) ratio is identical to within 15% for OHMs.

Galliano et al. (2008) also use both spline and multi-component profile fitting approaches to measure the PAH variations within galaxies; they show that both methods yield the same overall trends, although each have their own underlying biases depending on the property being measured. Given the large contributions of overlapping dust emission features to the 5–10 μm spectrum, which are not possible to separate from the underlying blackbody emission using spline fits (Marshall et al. 2007), we consider the PAHFIT results to be the more robust method. Measurements of PAH features in the literature, however, typically use a spline-fit method (*eg*, Brandl et al. 2006; Desai et al. 2007; Spoon et al. 2007; Zakamska et al. 2008). In particular, comparisons of PAH data from the OHM galaxies to other samples (*eg*, the "fork diagram" from Spoon et al. 2007) must use the same method to return physically meaningful results. While PAHFIT fluxes may thus better represent the absolute PAH luminosity, the spline-fit data are used when comparing the OHMs to objects from the literature (Table 7).

Water ice absorption at 6 μm can have significant effects on the measurement of the 6.2 μm PAH equivalent width (EW); following the method of Spoon et al. (2007), we correct for this by substituting the continuum inferred while measuring the 9.7 μm silicate strength for the measured 6.2 μm continuum (see §5.5). In total, 24 OHMs and three non-masing galaxies with SL data showed absorption strong enough to affect the measured EW; the spline fit with the new continuum decreased the EW for all objects except IRAS 11180+1623, for which the continuum levels as measured by the PAH fit and the silicate depth are nearly identical (within error). Since PAHFIT does not fit for ice absorption, we also calculate ice-corrected EW for objects showing absorption at 6 μm by using the flux from PAHFIT and the inferred continuum from silicate measurements.

The 11.3 μm PAH is seated atop the edge of the deep silicate absorption at 9.7 μm; determining an extinction-corrected continuum level for EW measurements is thus also difficult. Spectral mapping of AGN galaxies with ISOCAM has shown that PAH emission can be spatially extended and suppressed near the nucleus (Le Floc'h et al. 2001; Díaz-Santos et al. 2010); this means that the PAH emission in AGN may be largely unaffected by dust absorption. Starburst galaxies, however, can show strong PAH emission in both the 6.2 and 11.3 μm bands in the nuclear regions where the silicate optical depth is at its highest (Galliano et al. 2008), and is likely to affect continuum levels for PAH features. The measured 11.3 μm PAH data using the spline-fit method

TABLE 7
PAH EMISSION FEATURES IN LOW-RESOLUTION SPECTRA

Object	PAHFIT luminosity		PAHFIT EW			Spline-fit luminosity		Spline-fit EW		
	6.2 [log $L/L_\odot$]	11.3 [log $L/L_\odot$]	6.2 [μm]	6.2 ice [μm]	11.3 [μm]	6.2 [log $L/L_\odot$]	11.3 [log $L/L_\odot$]	6.2 [μm]	6.2 ice [μm]	11.3 [μm]
IRAS 01355−1814	9.81	9.42	2.25		0.49	9.07	8.97	0.14		0.26
IRAS 01418+1651	8.98	9.07	1.81		1.86	8.60	8.48	0.44		0.61
IRAS 01562+2528	9.59	9.71	2.07		2.22	9.23	9.43	0.37		0.86
IRAS 02524+2046	9.37	9.62	0.54		1.85	9.19	9.13	0.49		0.53
IRAS 03521+0028	9.78	9.60	1.67	0.36	0.81	9.41	9.29	0.43	0.36	0.60
IRAS 04121+0223	9.48	9.42	1.82	0.89	2.01	9.11	9.02	0.44	0.38	0.78
IRAS 04454−4838	10.07	9.90	23.53	0.05	1.31	8.26	8.42	0.07	0.05	1.07
IRAS 06487+2208	9.89	9.75	0.55		0.36	9.60	9.47	0.26		0.26
IRAS 07163+0817	9.21	9.12	12.82		1.30	8.93	8.84	0.58		0.77
IRAS 07572+0533	–	8.95	–		0.04	< 8.95	8.88	< 0.10		0.04
IRAS 08201+2801	10.03	9.52	2.83	0.39	0.57	9.41	9.33	0.19	0.09	0.71
IRAS 08449+2332	9.78	9.63	2.79		1.09	9.38	9.25	0.43		0.59
IRAS 08474+1813	9.37	9.20	2.33		1.41	8.72	8.82	0.23		1.40
IRAS 09039+0503	9.65	9.73	1.59	0.19	2.58	9.13	9.09	0.30	0.19	0.76
IRAS 09539+0857	10.2	10.06	6.38		6.50	8.91	8.96	0.11		1.09
IRAS 10035+2740	9.21	9.33	2.10		1.03	8.77	8.72	0.27		0.25
IRAS 10039−3338	10.96	10.32	2.90	0.01	8.28	8.72	8.94	0.01	0.01	0.72
IRAS 10173+0828	9.37	9.51	2.50		5.13	8.65	8.64	0.35		0.95
IRAS 10339+1548	9.30	9.63	0.71		0.85	9.14	9.23	0.42		0.44
IRAS 10378+1109	9.30	9.36	0.45	0.04	0.64	8.62	9.02	0.07	0.04	0.49
IRAS 10485−1447	9.73	9.19	1.64		0.47	8.73	8.84	0.09	0.08	0.36
IRAS 11028+3130	9.11	9.54	1.13		2.33	8.41	8.85	0.14		0.64
IRAS 11180+1623	9.69	9.44	5.87	0.97	0.95	9.02	9.07	0.24	0.26	0.57
IRAS 11524+1058	9.55	9.85	1.09		3.07	8.87	9.17	0.12		0.69
IRAS 12018+1941	9.85	9.44	0.25		0.08	9.58	9.06	0.17		0.05
IRAS 12032+1707	10.33	10.20	3.54	0.06	1.33	9.40	9.64	0.07	0.06	0.61
IRAS 12112+0305	9.62	9.35	4.39	0.37	0.76	9.27	9.02	0.61	0.37	0.52
IRAS 12540+5708	9.59	8.66	0.03		0.01	8.94	9.29	0.01		0.04
IRAS 13218+0552	–	–	–	–	–	< 9.79	9.50	< 0.01		< 0.03
IRAS 13428+5608	9.55	9.45	0.52	0.09	0.76	9.03	8.98	0.14	0.09	0.37
IRAS 13451+1232	9.34	9.34	0.06		0.04	8.23	8.76	0.01		0.01
IRAS 14059+2000	9.16	9.06	0.25		0.48	8.93	8.89	0.23		0.43
IRAS 14070+0525	10.37	10.31	1.86	0.01	2.41	8.92	9.63	0.02	0.01	0.83
IRAS 14553+1245	9.57	9.47	0.63		0.65	9.37	9.22	0.44		0.60
IRAS 15327+2340	10.45	10.03	91.96	0.16	8.23	8.89	8.67	0.30	0.17	0.64
IRAS 16090−0139	10.17	9.99	1.14	0.07	1.45	9.34	9.38	0.09	0.07	0.51
IRAS 16255+2801	9.54	9.14	0.94	0.50	1.02	8.95	8.58	0.16	0.13	0.37
IRAS 16300+1558	10.31	9.97	1.66	0.04	1.09	9.28	9.48	0.07	0.04	0.60
IRAS 17207−0014	10.01	9.86	3.58	0.45	2.75	9.52	9.24	0.50	0.45	0.76
IRAS 18368+3549	9.82	9.74	2.43		2.62	9.50	9.26	0.61		0.74
IRAS 18588+3517	9.84	9.67	1.85	0.56	1.65	9.45	9.25	0.41	0.23	0.82
IRAS 20100−4156	9.96	9.83	1.52	0.06	1.23	9.32	9.38	0.19	0.06	0.77
IRAS 20286+1846	9.44	9.45	1.58	0.63	2.26	8.93	8.86	0.41	0.20	0.91
IRAS 21077+3358	9.86	9.85	2.88		1.15	9.23	9.28	0.21		0.40
IRAS 21272+2514	9.66	9.60	1.97	0.15	1.73	9.11	8.97	0.34	0.15	0.56
IRAS 22055+3024	9.22	9.27	0.28		0.26	8.88	9.10	0.15		0.22
IRAS 22116+0437	10.27	9.85	3.16		0.75	9.34	9.38	0.08		0.40
IRAS 22491−1808	9.47	9.33	1.38	0.45	0.98	9.07	8.94	0.43	0.45	0.57
IRAS 23028+0725	...	...	...	...	...	...	...	...	...	...
IRAS 23233+0946	9.68	9.59	1.74	0.36	1.45	9.30	9.17	0.47	0.36	0.76
IRAS 23365+3604	9.80	9.63	2.37	0.27	0.92	9.31	9.18	0.35	0.27	0.43
IRAS 00163−1039	9.30	9.16	3.32		0.95	9.00	8.83	0.52		0.43
IRAS 01572+0009	9.86	9.47	0.10		0.04	9.60	9.55	0.07		0.06
IRAS 05083+7936	9.93	9.95	4.45		2.10	9.68	9.57	0.62		0.66
IRAS 06538+4628	8.75	8.77	1.00		0.60	8.51	8.50	0.45		0.36
IRAS 08559+1053	9.89	9.86	0.31	0.19	0.55	9.63	9.52	0.21	0.19	0.29
IRAS 09437+0317	9.10	9.16	1.47		1.99	8.89	8.82	0.62		0.77
IRAS 10565+2448	9.90	9.80	1.53		1.43	9.55	9.31	0.51		0.51
IRAS 11119+3257	9.92	9.68	0.04	0.05	0.04	9.93	8.36	0.06	0.05	0.003
IRAS 13349+2438	–	–	–	–	–	< 9.39	< 9.10	< 0.01		< 0.01
IRAS 15001+1433	9.86	9.86	0.30	0.14	0.43	9.54	9.44	0.16	0.14	0.20
IRAS 15206+3342	9.81	9.75	0.38		0.41	9.56	9.47	0.25		0.27
IRAS 20460+1925	...	...	...	...	...	...	...	...	...	...
IRAS 23007+0836	9.23	9.19	0.33		0.34	8.99	8.89	0.19		0.20
IRAS 23394−0353	9.26	9.16	2.24		2.47	8.94	8.72	0.53		0.64
IRAS 23498+2423	9.52	9.53	0.06		0.13	9.25	9.05	0.04		0.06

NOTE. — The "ice" 6.2 μm PAH columns use a continuum that is corrected for water ice absorption (where present) at 6 μm. – indicates that PAHFIT fit no significant flux for a particular dust component.

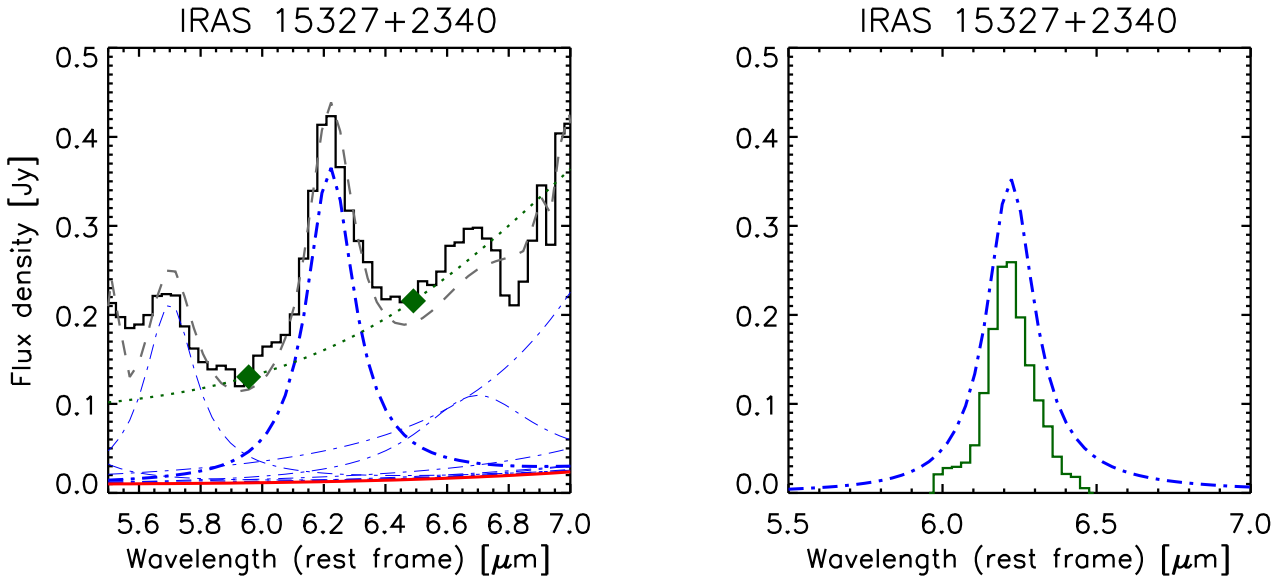

FIG. 7.— Differences between two methods used to measure PAH fluxes in IRS spectra, illustrated on the spectrum of IRAS 15327+2340 (Arp 220). (*left*): The observed spectrum centered on the 6.2 μm PAH feature is shown in black. The minimum at 5.9 μm is the result of absorption by water ice. For the spline method, the PAH feature is defined as the integrated flux above a spline-interpolated continuum (*green dotted line*) between 5.95 and 6.5 μm. The dot-dashed blue lines represent individual Drude fit components from PAHFIT, while the red line is the continuum emission (blackbody dust + starlight). The dashed grey line shows PAHFIT's global fit to the data. (*right*): PAHFIT (*blue*) and spline-fit (*green*) results with the continuum subtracted; the feature as measured by PAHFIT has significantly more flux than with the spline continuum, typical of nearly all galaxies in our sample.

are therefore likely to underestimate the luminosities.

5.5. *Absorption features*

5.5.1. *Silicates*

The LR spectra show near-ubiquitous absorption from amorphous silicate dust, with a strong feature caused by a Si-O stretching mode near 9.7 μm and a weaker feature caused by an Si-O-Si bending mode near 18 μm (Knacke & Thomson 1973). The presence of dust is unsurprising, as the characteristic extreme IR luminosities of ULIRGs are caused by large amounts of heated dust being thermally re-radiated. Hao et al. (2007) found that ULIRGs nearly uniformly show absorption in the two silicate features, in contrast to QSOs and some Seyfert galaxies which typically show the feature in emission (Siebenmorgen et al. 2005; Hao et al. 2005; Sturm et al. 2005; Schweitzer et al. 2008).

We measure the strength of the silicate absorption at both 9.7 and 18 μm using the method of Spoon et al. (2007):

$$S_\lambda = ln\left(\frac{f_\lambda}{f_{cont}}\right), \quad (5)$$

where f_λ is the measured flux and f_{cont} the interpolated continuum at the feature extremum. More negative values of S_{sil} represent deeper absorption. The expected continuum is calculated using a combination of spline and power-law fits, depending on the strength of the PAH and water ice features in the spectrum (Spoon et al. 2007).

All OHMs and $\sim$ 95% of the non-masing galaxies showed absorption at both 9.7 and 18 μm (Table 8); the average depth for the OHMs is $S_{9.7} = -1.8 \pm 0.8$, while the average depth of the non-masing galaxies is $S_{9.7} = -0.6 \pm 0.4$. The deepest absorption is in the OHM IRAS 04454-0838 ($S_{9.7} = -3.7$), while only one object (the non-masing galaxy IRAS 13349+2438) shows emission in both amorphous silicate features.

In addition to the amorphous silicate, we detect weaker features from crystalline silicate absorption in 19 OHMs, including bands at 11, 16, 19, 23, and 28 μm (see Figure 8 for an example). We use the method of Spoon et al. (2006) to subtract off both the dust continuum and amorphous component to measure the residual optical depth at 16 and 23 μm, typically the strongest crystalline features (Table 8). The deepest S_{16} occurs for IRAS 10039−3338, at −0.4; however, the S/N ratio means we are only sensitive to an absorption limit of $S_{16} \simeq -0.1$ and $S_{18} \simeq -0.05$. Only one detection of crystalline silicates is made in a non-masing galaxy, in IRAS 11119+3257. Since all detections of crystalline silicates in OHMs have $S_{9.7} < -1.4$, the lower total dust column in non-masing galaxies is a likely contributor to the detection rate.

5.5.2. *Aliphatic hydrocarbons*

Absorption bands arising from hydrogenated amorphous carbon grains (HACs) can also be significant contributors to diffuse dust in the galactic ISM (Chiar et al. 2000). ISO (Spoon et al. 2001, 2002) and *Spitzer* (Dartois et al. 2007; Dartois & Muñoz-Caro 2007) observations have identified HAC absorption features due to bending modes at 6.85 μm (CH_2/CH_3) and 7.25 μm (CH_3) in ULIRGs. These aliphatic features represent a counterpart to the aromatic hydrocarbons responsible for PAH emission and are an abundant component of the ISM in luminous galaxies.

We detect absorption from the 6.85 μm HAC transition in 27/51 galaxies in the OHM sample (Figure 8), with zero detections in the non-masing sample. The accopmanying 7.25 μm feature is detected in eight of the galaxies in which the 6.85 μm feature is seen. The strength of the HAC is measured using a spline fit with pivots at 5.2, 5.6, 7.8, 14.0, and 26.0 μm to determine the local continuum in the 6–8 μm region (Spoon et al. 2007) and integrate the total flux within the absorption feature (Table 8). The average optical depth of the 6.85 μm feature is $\tau_{6.85} = 0.23 \pm 0.11$, and the average depth of the 7.25 μm feature is $\tau_{7.25} = 0.20 \pm 0.06$. Many of the galaxies with no detection of HACs, however, have limits from noise that are consistent with the absorption depths measured in brighter galaxies.

5.5.3. *Ices*

Absorption from ices in a variety of molecular species (including H_2O, CO, CO_2, and CH_4) has been detected in spectroscopy of IR-bright galaxies (Spoon et al. 2000, 2001; Sturm et al. 2000). The band from water ice absorption stretching from 6–8 μm is prominent (Figure 8) and was detected in $\sim$ 10% of a sample of bright galaxies using ISO (Spoon et al. 2002) and the IRS (Armus et al. 2004; Spoon et al. 2005; Armus et al. 2007).

We detected water ice absorption at 6 μm in 24 OHMs and three non-masing galaxies. We use the spline continuum from fitting the 9.7 μm silicate feature as the local 5.5–7 μm continuum in order to obtain an optical depth spectrum for the 6 μm absorption complex. The resulting water ice optical depths are tabulated in Table 8. We note that contamination by 6.2 μm PAH emission and absorption by other species than water ice (Spoon et al. 2005) may add confusion in properly measuring optical depths.

5.5.4. *C_2H_2, HCN, and CO_2*

Previous mid-IR surveys have also identified bands of molecular gas absorption in ULIRGs (Spoon et al. 2006; Armus et al. 2007; Lahuis et al. 2007), including the vibration-rotation bands of acetylene (C_2H_2; 13.7 μm), hydrogen cyanide (HCN; 14.02 μm), and carbon dioxide (CO_2; 15.0 μm). Lahuis et al. (2007) reported the detection of both C_2H_2 and HCN in fifteen (U)LIRG nuclei, with detections of CO_2 in four objects. Eight of the objects in the Lahuis sample are OHMs in our sample; we confirm detections of C_2H_2 in all eight galaxies, in addition to the OHMs IRAS 10039-3338 and IRAS 12018+1941 (Figure 8). HCN is detected in only 4/10 archival galaxies, meaning that we cannot confirm the HCN detection of four galaxies; since the optical depth of HCN is typically much weaker than that of C_2H_2, however, it is possible that our lower detection rate is a result of improved S/N in their reduction process. We also confirm the detection of CO_2 in IRAS 15327+2340 (Arp 220). No galaxies in the non-masing control sample showed absorption in any molecular band, nor did any of the OHMs observed in our dedicated program.

Since these gas-phase absorption features are actually a blend of multiple absorption lines, the peak optical

TABLE 8
SOLID-PHASE ABSORPTION FEATURES

Object	6.0 μm H_2O ice	6.85 μm HAC		7.25 μm HAC		9.7 μm	18 μm	16 μm	23 μm
	τ	τ	flux	τ	flux	S_{sil}	S_{sil}	S_{sil}^{resid}	S_{sil}^{resid}
IRAS 01355−1814						−2.4	−0.9	−0.3	−0.2
IRAS 01418+1651		0.49	−8.3			−1.3	−0.4		
IRAS 01562+2528						−0.7	−0.3		
IRAS 02524+2046		0.20	−0.4			−0.9	−0.3		
IRAS 03521+0028	0.42	0.13	−0.4			−1.4	−0.2	−0.1	−0.1
IRAS 04121+0223	1.61					−1.0	−0.2		
IRAS 04454−4838	0.42	0.35	−9.0	0.10	−1.5	−3.7	−1.0	−0.3	−0.2
IRAS 06487+2208		0.23	−4.6			−1.2	−0.3		
IRAS 07163+0817						−1.2	−0.1		
IRAS 07572+0533						−0.6	−0.3		
IRAS 08201+2801	1.06	0.37	−4.0	0.22	−1.5	−2.2	−0.6	−0.2	−0.1
IRAS 08449+2332						−1.2	−0.5	−0.1	−0.1
IRAS 08474+1813		0.36	−0.2			−1.9	−1.2		
IRAS 09039+0503	0.98	0.15	−0.5			−2.0	−0.6		
IRAS 09539+0857		0.24	−2.5			−3.1	−1.2	−0.4	−0.2
IRAS 10035+2740						−1.5	−0.8		
IRAS 10039−3338	0.23	0.23	−166.3			−3.1	−1.0	−0.4	−0.3
IRAS 10173+0828						−1.9	−0.8	−0.3	−0.2
IRAS 10339+1548						−1.1	−0.05		
IRAS 10378+1109	0.72	0.18	−0.6			−2.0	−0.3		
IRAS 10485−1447		0.25	−0.4			−2.9	−0.9		
IRAS 11028+3130						−2.6	−1.0		
IRAS 11180+1623	0.54					−1.7	−0.5		
IRAS 11524+1058		0.27	−1.5	0.2:	−0.3:	−1.5	−0.8		
IRAS 12018+1941		0.16	−2.6			−1.4	−0.4		
IRAS 12032+1707	0.71	0.55	−6.6	0.30	−3.9	−2.7	−0.8		
IRAS 12112+0305	0.59	0.41	−3.5			−1.8	−0.3	−0.2	−0.1
IRAS 12540+5708						−0.7	−0.2		
IRAS 13218+0552						−0.5	−0.4		
IRAS 13428+5608	0.50	0.40	−28.5			−2.0	−0.5		
IRAS 13451+1232						−0.5	−0.1		
IRAS 14059+2000						−0.8	−0.1		
IRAS 14070+0525	0.90	0.24	−1.8	0.15	−1.8	−2.7	−0.9		
IRAS 14553+1245						−1.3	−0.5		
IRAS 15327+2340	0.68	0.35	−50.1			−3.1	−0.4	−0.2	−0.1
IRAS 16090−0139	0.56	0.45	−10.5	0.24	−5.6	−2.4	−0.6		
IRAS 16255+2801	0.54					−2.2	−0.6		
IRAS 16300+1558	0.61	0.38	−2.2	0.21	−1.1	−2.7	−0.7	−0.3	−0.1
IRAS 17207−0014	0.31	0.23	−17.4			−1.9	−0.6	−0.2	−0.1
IRAS 18368+3549						−1.8	−0.2	−0.3	−0.2
IRAS 18588+3517	0.72					−2.2	−0.6	−0.3	–
IRAS 20100−4156	1.45	0.23	−2.9	0.23	−4.5	−2.4	−0.7	−0.2	−0.1
IRAS 20286+1846	1.08					−1.6	−0.6		
IRAS 21077+3358						−1.9	−0.7		
IRAS 21272+2514	1.66	0.21	−0.7			−2.8	−0.7		
IRAS 22055+3024						−1.3	−0.3		
IRAS 22116+0437		0.04:	−0.1:			−2.6	−0.9	−0.2	−0.2
IRAS 22491−1808	0.43	0.19	−0.2			−1.5	−0.5	−0.2	–
IRAS 23028+0725	...	...	...	...	...	...	−0.6		
IRAS 23233+0946	0.44					−1.9	−0.4		
IRAS 23365+3604	0.66					−2.0	−0.5		
IRAS 00163−1039						−0.5	−0.1		
IRAS 01572+0009						−0.2	−0.2		
IRAS 05083+7936						−1.1	−0.3		
IRAS 06538+4628						−0.5	−0.2		
IRAS 08559+1053	0.18					−0.6	−0.2		
IRAS 09437+0317						−1.1	−0.3		
IRAS 10565+2448						−1.2	−0.3		
IRAS 11119+3257	0.19					−0.7	−0.3	−0.2	–
IRAS 13349+2438						0.1	0.07		
IRAS 15001+1433	0.30					−0.9	−0.4		
IRAS 15206+3342						−0.4	−0.2		
IRAS 20460+1925	...	...	...	...	...	...	−0.4		
IRAS 23007+0836						−0.3	−0.1		
IRAS 23394−0353						−0.7	−0.3		
IRAS 23498+2423						−0.6	−0.3		

NOTE. — Silicate strength is defined in Eqn. 5; the 9.7 and 18 μm features are depths for amorphous silicates, while the 16 and 23 μm crystalline features are residual depths measured after the 18 μm feature was subtracted. Fluxes are given in 10^{-21} W cm^{-2}; objects marked with a : represent uncertain detections.

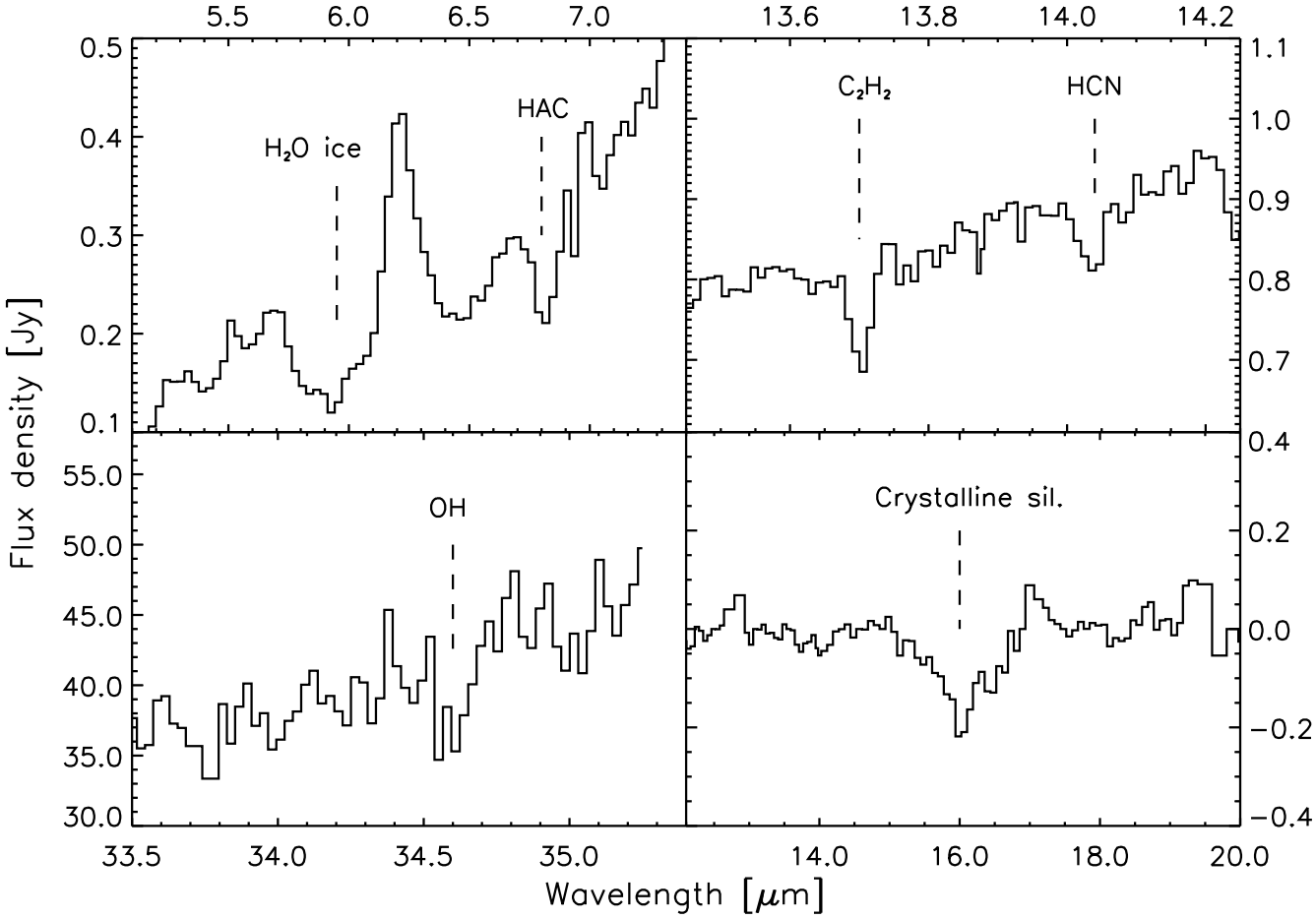

FIG. 8.— Examples of mid-IR absorption features for the OHM IRAS 15327+2340 (Arp 220). *Top left*: The 6.0 μm H_2O ice and 6.85 μm HAC absorption features. *Top right*: Gas-phase C_2H_2 13.7 μm and HCN 14.0 μm absorption. *Bottom left*: Gas-phase OH 34.6 μm absorption. *Bottom right*: Residual optical depth of the 16 μm crystalline silicate feature. Measurements for all labeled features are in Tables 8 and 9.

TABLE 9
Gas-phase absorption features

Object	13.7 μm C_2H_2		14.02 μm HCN		15.0 μm CO_2	
	f_{norm}	flux	f_{norm}	flux	f_{norm}	flux
IRAS 10039−3338	0.93	−0.9	0.86	−4.0		
IRAS 12018+1941	0.95	−0.7	0.94	−0.8		
IRAS 12540+5708	0.95	−9.5				
IRAS 13218+0552	0.82	−1.1				
IRAS 13428+5608	0.93	−0.8				
IRAS 14070+0525	0.79	−0.4				
IRAS 15327+2340	0.84	−5.8	0.90	−5.6	0.94	−2.0
IRAS 16090−0139	0.86	−1.1				
IRAS 17207−0014	0.93	−0.7				
IRAS 20100−4156	0.82	−1.4	0.84	−1.1		
IRAS 22491−1808	0.92	−0.7				

Note. — f_{norm} gives the peak depth of absorption features plotted in normalized flux units. Fluxes are measured in 10^{-21} W cm^{-2}.

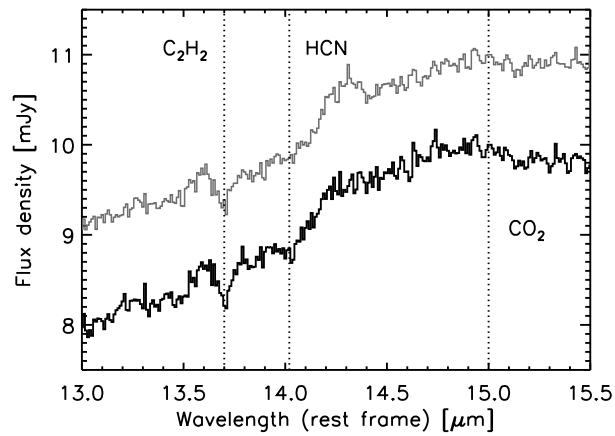

Fig. 9.— Medianed HR spectra for both OHMs (*black*) and non-masing (*grey*) galaxies, sampled at intervals of 0.01 μm and normalized in flux at 15 μm. PAH emission is visible in bands centered at 13.6 and 14.2 μm. The dotted lines mark locations of gas-phase absorption in C_2H_2 (13.7 μm), HCN (14.02 μm), and CO_2 (15.0 μm). The spectra are vertically offset to highlight the differences between the samples.

depth measured is a function of the velocity resolution of the spectrograph. We therefore report the integrated flux and the peak depth in normalized flux units (f_{norm}, where the spectrum has been divided by the adopted continuum; Spoon et al. 2004) in Table 9.

Lahuis et al. (2007) model abundances for ULIRGs with detections of C_2H_2, HCN, and CO_2, and suggest that they are associated with a phase of deeply embedded star formation, excluding the possibility of the features arising from an X-ray dominated region (XDR) powered by AGN. Darling (2007) has also shown that OHMs have the highest mean molecular gas densities among starburst galaxies (traced by the $J = 1 \rightarrow 0$ rotational HCN transition) and also possess high dense molecular gas fractions, comprising a distinct population in the IR-CO relation. The results of Lahuis et al. (2007) show that 9/15 ULIRGs with absorption in both C_2H_2 and HCN are known OHMs in our *Spitzer* sample; this dense gas fraction ($\sim$ 50%) is nearly identical to the observed OHM fraction in starbursts with dense (ULIRGs with $L_{HCN}/L_{CO} > 0.07$) fractions of molecular gas (Gao & Solomon 2004b; Darling 2007; Baan et al. 2008).

Given that the S/N ratio for the OHM and non-masing galaxies are of comparable magnitude, the lack of detection of any gas-phase species in the non-masing galaxies is a striking difference compared to the OHMs. Figure 9 shows the median stack of both samples near the regions of gas-phase absorption; while the C_2H_2 feature at 13.7 μm can be clearly seen in the median OHM spectrum, neither the HCN nor the CO_2 transition is prominent. Since the data have been median stacked (as opposed to a mean, which can be dominated by a few deep absorbers), this suggests low-levels of C_2H_2 present in a significant fraction of the OHM host galaxies. No molecular absorption appears in the medianed spectrum for the non-masing galaxies.

While a connection between OHMs and dense molecular gas is known to exist, the lack of detected molecular absorption in the mid-IR for the majority of OHMs is not entirely unexpected. OHMs occur in merging galaxies where different populations of gas may be kinematically and thermally distinct, yet are observed as a single unresolved region within the *Spitzer* beam. Lahuis et al. (2007) suggest that high abundances of warm, dense gas are associated with deeply-embedded star formation, where HII regions are prevented from expanding by large pressure gradients and extend the lifetime of the star formation process.

Baan et al. (2008) interpret dense gas abundances as excluding very hard radiation fields (such as those found in XDRs) that dissociate the molecules; they suggest that the molecular emission arises from PDRs surrounding HII regions. Although few OHMs show absorption from dense molecular gas, the OHM sample also has few identified AGN or XDRs (only 4/51 OHMs show [Ne V] at 14 μm). The connection between dense molecular gas and the presence of an AGN is thus unclear based on this data alone.

5.5.5. *Gas-phase OH*

For three OHMs, we report detection of the $^2\Pi_{1/2}$ J=5/2 $\rightarrow$ $^2\Pi_{3/2}$ J=3/2 OH absorption doublet near 34.616 μm: III Zw 35 (IRAS 01418+1651), Mrk 273 (IRAS 13428+5608), and Arp 220 (IRAS 15327+2340). This feature is generally difficult to detect since it lies near the noisy, far-red edge of the LH module; for all objects with $z > 0.08$, it is redshifted out of the IRS range. OH absorption at 34.6 μm in Arp 220 was first reported by Skinner et al. (1997) using ISO and confirmed with the IRS by Farrah et al. (2007), who incorrectly identified it as the OH^- ion. All OH absorption features are well fit with a single Gaussian, since the separation between the doublet features ($\Delta\lambda \simeq 0.02$ μm) is comparable to the resolution element in the LH module. No detection of OH absorption was made for any of the non-masing galaxies.

Assuming the OH transitions are optically thin, we can use the EW to derive a column density for the OH ground state, which is likely to be a good proxy for the total column at typical molecular cloud densities (Bradford et al. 1999):

$$N_l = \frac{EW}{A_{ul}} \frac{8\pi c}{\lambda^4} \frac{g_l}{g_u}. \quad (6)$$

OH column densities for all galaxies are quite similar,

TABLE 10
PROPERTIES OF OH GAS-PHASE ABSORPTION

OHM	f_{OH} [10^{-21} W cm^{-2}]	τ_{peak}	EW [10^{-3} μm]	N_{OH} [cm^{-2}]	γ_{abs} [ph/s]	γ_{OHM} [ph/s]	ϕ_{pump} %
IRAS 01418+1651 (III Zw 35)	−6.1	0.15	5.5	1.1×10^{17}	1.7×10^{54}	1.8×10^{53}	10
IRAS 13428+5608 (Mrk 273)	−28.5	0.14	10.2	2.1×10^{17}	1.7×10^{55}	1.4×10^{53}	0.8
IRAS 15327+2340 (Arp 220)	−172	0.21	15.0	3.0×10^{17}	2.3×10^{55}	1.6×10^{53}	0.7

NOTE. — The pumping efficiency ($\phi_{pump} = \gamma_{OHM}/\gamma_{abs} \times 100$) assumes all pumping comes from the 34.6 μm transition.

lying between $(1-3) \times 10^{17}$ cm^{-2} (Table 10). The measured N_{OH} from the IRS data for Arp 220 also agrees within a factor of 2 of the column measured with ISO (Skinner et al. 1997). Limits for galaxies in which the 34.6 μm OH feature is not detected are of order $N_{OH} \lesssim 1 \times 10^{17}$ cm^{-2}.

We compare the N_{OH} derived from the rotational 34.6 μm transitions to the OH column density measured in galaxies who show the hyperfine 1667 MHz feature in absorption. The majority of such galaxies are ULIRGs of comparable luminosity to the galaxies in our non-masing sample. Measurements from ten OH absorbers (Baan et al. 1992; Darling 2007) give $N_{OH} = T_{ex}(1.8 \pm 1.9) \times 10^{15}$ cm^{-2}, where T_{ex} is the OH excitation temperature in K. If the dust and gas are well-mixed, then the temperature of the dust ($\sim 50-100$ K) can be used as a proxy for T_{ex}. This gives OH column densities for both OHMs (34.6 μm) and non-masing galaxies (1667 MHz) with comparable values of $N_{OH} \simeq 10^{17}$ cm^{-2}. If so, then this addresses one of the crucial differences between OHMs and non-masing ULIRGs - namely, that differences in the abundance of masing molecules are *not* a key factor for triggering an OHM.

The amount of OH available in the galaxy can also test models of the OHM pumping mechanism. Skinner et al. (1997) computed the photon flux ($\gamma_{abs} = L_{abs}^{OH}/h\nu_{OH}$) absorbed in the 34.6 μm transition from the OHM Arp 220. They found that γ_{abs} is roughly 1% of the photon flux in the OHM ($\gamma_{OHM} = L_{OHM}/h\nu_{OHM}$). If the 18-cm and mid-IR pumping photons lie along the same line of sight, this means that pumping photons from the 34.6 μm transition alone can power the OHM (given an efficiency of $\sim 1\%$ or higher). While radiative transfer models from Lockett & Elitzur (2008) suggest that the 53 μm OH transition likely contributes more pumping photons than the 34.6 μm line, the energetics are consistent with the basic acccepted mid-IR pumping model.

For the galaxies in our sample with OH absorption, Arp 220 and Mrk 273 would require pumping efficiencies on the order of 1% to power the OHMs from the 34.6 μm transition alone. III Zw 35 shows the weakest OH absorption among our detections and would require an efficiency of $\phi_{pump} \simeq 10\%$.

6. CONCLUSIONS

We present mid-infrared spectra and photometry for 51 OH megamasers taken with the IRS on *Spitzer*, along with 15 galaxies confirmed to have **no** megamaser emission above $L_{OH} = 10^{2.3} L_{\odot}$. All objects in both samples have full coverage in both the low- and high-resolution IRS modules. We measure both emission (PAH, H_2, and fine-structure atomic transitions) and absorption (silicates, hydrogenated amorphous carbon grains, and molecular bands) features, with full spectra, line fluxes, equivalent widths, and absorption depths presented for each object.

The majority of the galaxies closely resemble standard mid-IR ULIRG templates, with the low-resolution emission dominated by moderate-to-deep amorphous silicate absorption at 9.7 and 18 μm and PAH features at 6.2, 7.7, 8.6, 11.3 and 12.7 μm. The OHMs (on average) show deeper silicate absorption and steeper continuum slopes than the non-masing galaxies. Crystalline silicate absorption is detected in roughly a third of OHMs, but in only 1 out of 15 non-masing galaxies. OHMs are also the only galaxies in our sample to show absorption from hydrogenated amorphous carbon (HAC), gas-phase HCN, C_2H_2, and CO_2; however, higher average noise in the non-masing spectra mean that features at similar absorption depths could be obscured due to lack of sensitivity. High-resolution spectra show emission from [Ne II] and [Ne III] in almost all galaxies, with emission from [S III], [S IV], and [O IV] commonly detected. The high-ionization [Ne V] line (a clear tracer of AGN) is detected in $< 10\%$ of OHMs and in 53% of the non-masing galaxies. Almost all galaxies in both samples also show emission in multiple H_2 rotational transitions.

We also measure the 34.6 μm OH transition in three OHMs. OH column densities derived from the mid-IR OH transition are of the same order of magnitude as the column densities derived from the 1667 MHz OH transition for ULIRGs in the literature. We interpret this as evidence that the OH abundances in both OHMs and non-masing galaxies are similar, and are not a limiting factor for megamaser emission.

A companion paper (Willett et al. 2011; Paper II) presents a full analysis of the mid-IR data, with comparisons between the two samples and connections to the OH megamaser properties.

This work is based on observations made with the Spitzer Space Telescope, which is operated by the Jet Propulsion Laboratory, California Institute of Technology under a contract with NASA. Support for this work was provided by NASA through grant 30407 issued by JPL/Caltech. We have made extensive use of the NASA/IPAC Extragalactic Database (NED) which is operated by JPL and Caltech under contract with NASA. Many thanks are due to J.-D. Smith for help with PAHFIT, N. Halverson for comments on computing flux limits, D. Farrah for useful discussions, and to the Spitzer Science Center for hosting KWW and JD in April 2007. VC acknowledges partial support from the EU ToK grant 39965 and FP7-REGPOT 206469.

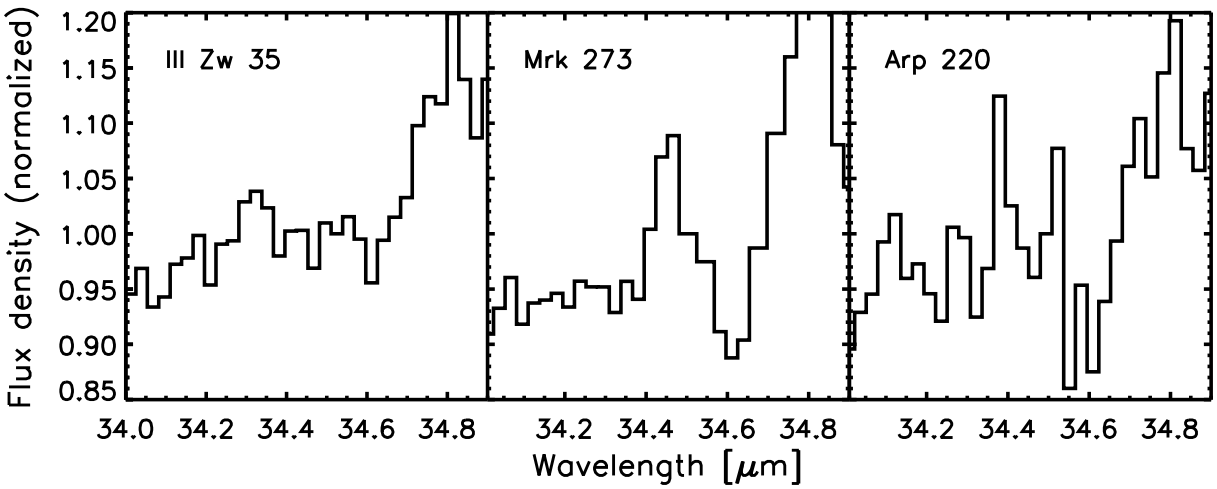

FIG. 10.— The 34.6 μm OH absorption feature in III Zw 35, Mrk 273, and Arp 220. All spectra are been normalized in flux near 34.5 μm.

APPENDIX

HIGH-RESOLUTION DATA WITH BACKGROUND SKY SUBTRACTION

As discussed in §3, the reduction process for the overall sample is slightly different for some archival galaxies that did not have separate IRS sky backgrounds in the high-resolution modules. Since much of our subsequent analysis (Paper II) depends on statistical comparisons between the two samples, we chose to minimize possible systematic errors and reduced all galaxies in a uniform manner *without* HR sky subtraction. These data are, however, likely to be a more reliable indicator of the absolute flux levels due to subtraction of the zodiacal background; therefore, we also present atomic and molecular line fluxes for these galaxies.

REFERENCES

Armus, L., Charmandaris, V., Bernard-Salas, J., Spoon, H. W. W., Marshall, J. A., Higdon, S. J. U., Desai, V., Teplitz, H. I., Hao, L., Devost, D., Brandl, B. R., Wu, Y., Sloan, G. C., Soifer, B. T., Houck, J. R., & Herter, T. L. 2007, ApJ, 656, 148

Armus, L., Charmandaris, V., Spoon, H. W. W., Houck, J. R., Soifer, B. T., Brandl, B. R., Appleton, P. N., Teplitz, H. I., Higdon, S. J. U., Weedman, D. W., Devost, D., Morris, P. W., Uchida, K. I., van Cleve, J., Barry, D. J., Sloan, G. C., Grillmair, C. J., Burgdorf, M. J., Fajardo-Acosta, S. B., Ingalls, J. G., Higdon, J., Hao, L., Bernard-Salas, J., Herter, T., Troeltzsch, J., Unruh, B., & Winghart, M. 2004, ApJS, 154, 178

Baan, W. A., Haschick, A., & Henkel, C. 1992, AJ, 103, 728

Baan, W. A., Henkel, C., Loenen, A. F., Baudry, A., & Wiklind, T. 2008, A&A, 477, 747

Baan, W. A., Wood, P. A. D., & Haschick, A. D. 1982, ApJ, 260, L49

Bradford, C. M., Stacey, G. J., Fischer, J., Smith, H. A., Cohen, R. J., Greenhouse, M. A., Lord, S. D., Lutz, D., Maiolino, R., Malkan, M. A., & Rieu, N. Q. 1999, in ESA Special Publication, Vol. 427, The Universe as Seen by ISO, ed. P. Cox & M. Kessler, 861–+

Brandl, B. R., Bernard-Salas, J., Spoon, H. W. W., Devost, D., Sloan, G. C., Guilles, S., Wu, Y., Houck, J. R., Weedman, D. W., Armus, L., Appleton, P. N., Soifer, B. T., Charmandaris, V., Hao, L., Higdon, J. A. M. S. J., & Herter, T. L. 2006, ApJ, 653, 1129

Chiar, J. E., Tielens, A. G. G. M., Whittet, D. C. B., Schutte, W. A., Boogert, A. C. A., Lutz, D., van Dishoeck, E. F., & Bernstein, M. P. 2000, ApJ, 537, 749

Condon, J. J., Cotton, W. D., Greisen, E. W., Yin, Q. F., Perley, R. A., Taylor, G. B., & Broderick, J. J. 1998, AJ, 115, 1693

Darling, J. 2007, ApJ, 669, L9

Darling, J., & Giovanelli, R. 2000, AJ, 119, 3003

—. 2001, AJ, 121, 1278

—. 2002a, AJ, 124, 100

—. 2002b, ApJ, 572, 810

Dartois, E., Geballe, T. R., Pino, T., Cao, A.-T., Jones, A., Deboffle, D., Guerrini, V., Bréchignac, P., & D'Hendecourt, L. 2007, A&A, 463, 635

Dartois, E., & Muñoz-Caro, G. M. 2007, A&A, 476, 1235

Desai, V., Armus, L., Spoon, H. W. W., Charmandaris, V., Bernard-Salas, J., Brandl, B. R., Farrah, D., Soifer, B. T., Teplitz, H. I., Ogle, P. M., Devost, D., Higdon, S. J. U., Marshall, J. A., & Houck, J. R. 2007, ApJ, 669, 810

Díaz-Santos, T., Charmandaris, V., Armus, L., Petric, A. O., Howell, J. H., Murphy, E. J., Mazzarella, J. M., Veilleux, S., Bothun, G., Inami, H., Appleton, P. N., Evans, A. S., Haan, S., Marshall, J. A., Sanders, D. B., Stierwalt, S., & Surace, J. A. 2010, ApJ, 723, 993

Draine, B. T. 2003, ARA&A, 41, 241

Farrah, D., Bernard-Salas, J., Spoon, H. W. W., Soifer, B. T., Armus, L., Brandl, B., Charmandaris, V., Desai, V., Higdon, S., Devost, D., & Houck, J. 2007, ApJ, 667, 149

Galliano, F., Madden, S. C., Tielens, A. G. G. M., Peeters, E., & Jones, A. P. 2008, ApJ, 679, 310

Gao, Y., & Solomon, P. M. 2004a, ApJS, 152, 63

—. 2004b, ApJ, 606, 271

Genzel, R., Lutz, D., Sturm, E., Egami, E., Kunze, D., Moorwood, A. F. M., Rigopoulou, D., Spoon, H. W. W., Sternberg, A., Tacconi-Garman, L. E., Tacconi, L., & Thatte, N. 1998, ApJ, 498, 579

Hao, L., Spoon, H. W. W., Sloan, G. C., Marshall, J. A., Armus, L., Tielens, A. G. G. M., Sargent, B., van Bemmel, I. M., Charmandaris, V., Weedman, D. W., & Houck, J. R. 2005, ApJ, 625, L75

Hao, L., Weedman, D. W., Spoon, H. W. W., Marshall, J. A., Levenson, N. A., Elitzur, M., & Houck, J. R. 2007, ApJ, 655, L77

Henkel, C., Guesten, R., & Baan, W. A. 1987, A&A, 185, 14

Henkel, C., & Wilson, T. L. 1990, A&A, 229, 431

Higdon, S. J. U., Armus, L., Higdon, J. L., Soifer, B. T., & Spoon, H. W. W. 2006, ApJ, 648, 323

TABLE 11
Hi-res line fluxes for common atomic emission lines with HR sky subtraction

Object	[S IV] 10.511 μm	[Ne II] 12.814 μm	[Ne III] 15.555 μm	[S III] 18.713 μm
IRAS 01562+2528	–	–	–	0.65
IRAS 02524+2046	–	–	–	0.47
IRAS 04121+0223	–	–	–	0.67
IRAS 04454−4838	0.42	1.95	0.43	–
IRAS 06487+2208	–	–	–	5.01
IRAS 07163+0817	–	–	–	1.34
IRAS 08201+2801	–	–	–	0.41
IRAS 08449+2332	–	–	–	1.60
IRAS 08474+1813	–	–	–	0.14
IRAS 10035+2740	–	–	–	0.35
IRAS 10039−3338	0.98	17.22	4.20	8.08
IRAS 10339+1548	–	–	–	0.97
IRAS 11180+1623	–	–	–	0.40
IRAS 11524+1058	–	–	–	0.27
IRAS 12540+5708	–	19.47	–	–
IRAS 14059+2000	–	–	–	0.59
IRAS 14553+1245	–	–	–	1.58
IRAS 15327+2340	–	59.39	6.73	7.54
IRAS 16255+2801	–	–	–	1.54
IRAS 18368+3549	–	–	–	1.01
IRAS 18588+3517	–	–	–	2.89
IRAS 20286+1846	–	–	–	0.48
IRAS 21077+3358	–	–	–	0.74
IRAS 21272+2514	–	2.22	0.33	0.40
IRAS 22055+3024	–	–	–	1.16
IRAS 22116+0437	–	–	–	0.90
IRAS 00163−1039	2.64	87.43	14.30	32.10
IRAS 05083+7936	–	49.95	7.63	19.60
IRAS 06538+4628	0.84	47.34	5.90	20.49
IRAS 09437+0317	–	8.72	1.22	3.58
IRAS 23394−0353	–	46.45	7.60	18.50

Note. — Fluxes are in 10^{-21} W cm^{-2}. No data is given for the 26 OHMs in our program for lines with $\lambda_{rest} \lesssim 16$ μm since we have no SH sky subtraction available for these objects.

TABLE 12
Hi-res line fluxes for rarer atomic emission lines with HR sky subtraction

Object λ_{rest} [μm]	H I 7-6 12.368	[Ne V] 14.322	[Cl II] 14.369	[Fe II] 17.936	[Ne V] 24.318	[O IV] 25.890	[Fe II] 25.988	[S III] 33.481	[Si II] 34.815
IRAS 04454−4838	–	–	–	–	–	1.12	–	0.90	–
IRAS 06487+2208	–	–	–	–	–	1.12	–	–	–
IRAS 07163+0817	–	–	–	0.73	–	–	–	–	–
IRAS 10339+1548	–	–	–	–	0.84	2.55	–	–	–
IRAS 11524+1058	–	–	–	0.35	–	0.59	–	–	–
IRAS 14553+1245	–	–	–	0.41	–	–	–	–	–
IRAS 16255+2801	–	–	–	–	–	0.46	–	–	–
IRAS 18368+3549	–	–	–	0.51	–	–	–	–	–
IRAS 21272+2514	0.20	0.10	–	–	–	–	–	–	–
IRAS 00163−1039	0.64	–	–	–	–	1.56	2.46	32.18	74.28
IRAS 05083+7936	–	0.58	0.43	–	–	1.53	1.97	29.34	43.28
IRAS 06538+4628	–	1.08	–	1.06	–	–	2.15	37.21	48.72
IRAS 09437+0317	–	–	–	–	–	0.47	0.68	9.60	22.74
IRAS 23394−0353	0.59	–	–	–	–	1.49	2.53	42.37	53.56

Note. — Fluxes are in 10^{-21} W cm^{-2}. No data is given for the 26 OHMs in our program for lines with $\lambda_{rest} \lesssim 16$ μm since we have no SH sky subtraction available for these objects.

TABLE 13
Hi-res line fluxes and upper limits for H_2 transitions with HR sky subtraction

Object λ_{rest} [μm]	H_2 S(3) 9.67	H_2 S(2) 12.28	H_2 S(1) 17.04	H_2 S(0) 28.22
IRAS 01562+2528	–	–	0.78	–
IRAS 02524+2046	–	–	0.72	–
IRAS 04454−4838	1.05	1.21	3.03	0.76
IRAS 06487+2208	–	–	2.03	–
IRAS 08201+2801	–	–	0.51	–
IRAS 08449+2332	–	–	1.40	–
IRAS 08474+1813	–	–	0.27	–
IRAS 10035+2740	–	–	1.16	–
IRAS 10039−3338	3.39	1.79	3.85	–
IRAS 10339+1548	–	–	0.46	–
IRAS 11180+1623	–	–	0.89	–
IRAS 11524+1058	–	–	0.81	–
IRAS 12540+5708	2.42	4.22	–	–
IRAS 14059+2000	–	–	2.55	–
IRAS 15327+2340	–	7.36	15.42	14.55
IRAS 16255+2801	–	–	0.55	–
IRAS 21077+3358	–	–	1.17	–
IRAS 21272+2514	0.26	0.35	0.68	–
IRAS 22116+0437	–	–	1.35	–
IRAS 23028+0725	–	–	1.11	–
IRAS 00163−1039	2.18	2.82	6.01	–
IRAS 05083+7936	2.34	2.64	5.11	–
IRAS 06538+4628	–	3.33	8.70	2.99
IRAS 09437+0317	–	–	2.67	1.78
IRAS 23394−0353	3.40	2.25	4.99	1.38

Note. — Fluxes are in 10^{-21} W cm^{-2}. No data is given for the 26 OHMs in our program for the S(2) or S(3) lines since we have no SH sky subtraction available for these objects.

Higdon, S. J. U., Devost, D., Higdon, J. L., Brandl, B. R., Houck, J. R., Hall, P., Barry, D., Charmandaris, V., Smith, J. D. T., Sloan, G. C., & Green, J. 2004, PASP, 116, 975
Hinshaw, G., Weiland, J. L., Hill, R. S., Odegard, N., Larson, D., Bennett, C. L., Dunkley, J., Gold, B., Greason, M. R., Jarosik, N., Komatsu, E., Nolta, M. R., Page, L., Spergel, D. N., Wollack, E., Halpern, M., Kogut, A., Limon, M., Meyer, S. S., Tucker, G. S., & Wright, E. L. 2009, ApJS, 180, 225
Houck, J. R., Roellig, T. L., van Cleve, J., Forrest, W. J., Herter, T., Lawrence, C. R., Matthews, K., Reitsema, H. J., Soifer, B. T., Watson, D. M., Weedman, D., Huisjen, M., Troeltzsch, J., Barry, D. J., Bernard-Salas, J., Blacken, C. E., Brandl, B. R., Charmandaris, V., Devost, D., Gull, G. E., Hall, P., Henderson, C. P., Higdon, S. J. U., Pirger, B. E., Schoenwald, J., Sloan, G. C., Uchida, K. I., Appleton, P. N., Armus, L., Burgdorf, M. J., Fajardo-Acosta, S. B., Grillmair, C. J., Ingalls, J. G., Morris, P. W., & Teplitz, H. I. 2004, ApJS, 154, 18
Imanishi, M., Dudley, C. C., Maiolino, R., Maloney, P. R., Nakagawa, T., & Risaliti, G. 2007, ApJS, 171, 72
Kent, B., Braatz, J., & Darling, J. 2002, in Bulletin of the American Astronomical Society, Vol. 34, 1194–+
Knacke, R. F., & Thomson, R. K. 1973, PASP, 85, 341
Lahuis, F., Spoon, H. W. W., Tielens, A. G. G. M., Doty, S. D., Armus, L., Charmandaris, V., Houck, J. R., Stäuber, P., & van Dishoeck, E. F. 2007, ApJ, 659, 296
Le Floc'h, E., Mirabel, I. F., Laurent, O., Charmandaris, V., Gallais, P., Sauvage, M., Vigroux, L., & Cesarsky, C. 2001, A&A, 367, 487
Lockett, P., & Elitzur, M. 2008, ApJ, 677, 985
Lutz, D., Spoon, H. W. W., Rigopoulou, D., Moorwood, A. F. M., & Genzel, R. 1998, ApJ, 505, L103
Marshall, J. A., Herter, T. L., Armus, L., Charmandaris, V., Spoon, H. W. W., Bernard-Salas, J., & Houck, J. R. 2007, ApJ, 670, 129
Peeters, E., Spoon, H. W. W., & Tielens, A. G. G. M. 2004, ApJ, 613, 986
Rigopoulou, D., Kunze, D., Lutz, D., Genzel, R., & Moorwood, A. F. M. 2002, A&A, 389, 374
Roussel, H., Helou, G., Hollenbach, D. J., Draine, B. T., Smith, J. D., Armus, L., Schinnerer, E., Walter, F., Engelbracht, C. W., Thornley, M. D., Kennicutt, R. C., Calzetti, D., Dale, D. A., Murphy, E. J., & Bot, C. 2007, ApJ, 669, 959
Sanders, D. B., Mazzarella, J. M., Kim, D.-C., Surace, J. A., & Soifer, B. T. 2003, AJ, 126, 1607
Sanders, D. B., & Mirabel, I. F. 1996, ARA&A, 34, 749
Schweitzer, M., Groves, B., Netzer, H., Lutz, D., Sturm, E., Contursi, A., Genzel, R., Tacconi, L. J., Veilleux, S., Kim, D., Rupke, D., & Baker, A. J. 2008, ApJ, 679, 101
Schweitzer, M., Lutz, D., Sturm, E., Contursi, A., Tacconi, L. J., Lehnert, M. D., Dasyra, K. M., Genzel, R., Veilleux, S., Rupke, D., Kim, D.-C., Baker, A. J., Netzer, H., Sternberg, A., Mazzarella, J., & Lord, S. 2006, ApJ, 649, 79
Siebenmorgen, R., Haas, M., Krügel, E., & Schulz, B. 2005, A&A, 436, L5
Skinner, C. J., Smith, H. A., Sturm, E., Barlow, M. J., Cohen, R. J., & Stacey, G. J. 1997, Nature, 386, 472
Smith, J. D. T., Draine, B. T., Dale, D. A., Moustakas, J., Kennicutt, Jr., R. C., Helou, G., Armus, L., Roussel, H., Sheth, K., Bendo, G. J., Buckalew, B. A., Calzetti, D., Engelbracht, C. W., Gordon, K. D., Hollenbach, D. J., Li, A., Malhotra, S., Murphy, E. J., & Walter, F. 2007, ApJ, 656, 770
Solomon, P. M., Downes, D., Radford, S. J. E., & Barrett, J. W. 1997, ApJ, 478, 144
Spoon, H. W. W., Armus, L., Cami, J., Tielens, A. G. G. M., Chiar, J. E., Peeters, E., Keane, J. V., Charmandaris, V., Appleton, P. N., Teplitz, H. I., & Burgdorf, M. J. 2004, ApJS, 154, 184
Spoon, H. W. W., Keane, J. V., Cami, J., Lahuis, F., Tielens, A. G. G. M., Armus, L., & Charmandaris, V. 2005, in IAU Symposium, Vol. 231, Astrochemistry: Recent Successes and Current Challenges, ed. D. C. Lis, G. A. Blake, & E. Herbst, 281–290
Spoon, H. W. W., Keane, J. V., Tielens, A. G. G. M., Lutz, D., & Moorwood, A. F. M. 2001, A&A, 365, L353
Spoon, H. W. W., Keane, J. V., Tielens, A. G. G. M., Lutz, D., Moorwood, A. F. M., & Laurent, O. 2002, A&A, 385, 1022
Spoon, H. W. W., Koornneef, J., Moorwood, A. F. M., Lutz, D., & Tielens, A. G. G. M. 2000, A&A, 357, 898
Spoon, H. W. W., Marshall, J. A., Houck, J. R., Elitzur, M., Hao, L., Armus, L., Brandl, B. R., & Charmandaris, V. 2007, ApJ, 654, L49
Spoon, H. W. W., Tielens, A. G. G. M., Armus, L., Sloan, G. C., Sargent, B., Cami, J., Charmandaris, V., Houck, J. R., & Soifer, B. T. 2006, ApJ, 638, 759
Staveley-Smith, L., Norris, R. P., Chapman, J. M., Allen, D. A., Whiteoak, J. B., & Roy, A. L. 1992, MNRAS, 258, 725
Sturm, E., Lutz, D., Tran, D., Feuchtgruber, H., Genzel, R., Kunze, D., Moorwood, A. F. M., & Thornley, M. D. 2000, A&A, 358, 481
Sturm, E., Schweitzer, M., Lutz, D., Contursi, A., Genzel, R., Lehnert, M. D., Tacconi, L. J., Veilleux, S., Rupke, D. S., Kim, D.-C., Sternberg, A., Maoz, D., Lord, S., Mazzarella, J., & Sanders, D. B. 2005, ApJ, 629, L21
Weedman, D. W., Hao, L., Higdon, S. J. U., Devost, D., Wu, Y., Charmandaris, V., Brandl, B., Bass, E., & Houck, J. R. 2005, ApJ, 633, 706
Weedman, D. W., & Houck, J. R. 2009, ApJ, 693, 370
Werner, M. W., Roellig, T. L., Low, F. J., Rieke, G. H., Rieke, M., Hoffmann, W. F., Young, E., Houck, J. R., Brandl, B., Fazio, G. G., Hora, J. L., Gehrz, R. D., Helou, G., Soifer, B. T., Stauffer, J., Keene, J., Eisenhardt, P., Gallagher, D., Gautier, T. N., Irace, W., Lawrence, C. R., Simmons, L., Van Cleve, J. E., Jura, M., Wright, E. L., & Cruikshank, D. P. 2004, ApJS, 154, 1
Zakamska, N. L., Gómez, L., Strauss, M. A., & Krolik, J. H. 2008, AJ, 136, 1607